Newton-Krylov continuation of amplitude-modulated rotating waves in sheared annular electroconvection

Gregory M. Lewis* and Jamil Jabbour

Faculty of Science, University of Ontario Institute of Technology,

2000 Simcoe Street North, Oshawa, Ontario, Canada, L1G 0C5

M.C. Pugh

Department of Mathematics, University of Toronto,

40 St. George St., Toronto, Ontario, Canada, M5S 2E4

Stephen W. Morris

Department of Physics, University of Toronto,

60 St. George St., Toronto, Ontario, Canada, M5S 1A7

(Dated: July 3, 2024)

Abstract

We present an approach for studying the primary, secondary and tertiary flow transitions in sheared annular electroconvection. In particular, we describe a Newton-Krylov method based on time-integration for the computation of rotating waves and amplitude-modulated rotating waves, and for the continuation of these flows as a parameter of the system is varied. The method exploits the rotational nature of the flows, and requires only a time-stepping code of the model differential equations, i.e., it does not require an explicit code for the discretization of the linearized equations. The linear stability of the solutions is computed to identify the parameter values at which the transitions occur.

We apply the method to a model of electroconvection that simulates the flow of a liquid crystal film in the smectic A phase suspended between two annular electrodes, and subjected to an electric potential difference and a radial shear. Due to the layered structure of the smectic A phase, the fluid can be treated as two-dimensional and is modeled using the 2-D incompressible Navier-Stokes equations coupled with an equation for charge continuity. The system is a close analogue to laboratory-scale geophysical fluid experiments, and thus represents an ideal system in which to apply the method before its application to these other systems that exhibit similar flow transitions.

In the model for electroconvection, we identify the parameter values at which the primary transition from steady axisymmetric flow to rotating waves occurs, as well as at which the secondary transition from the rotating waves to amplitude-modulated rotating waves occurs. In addition, we locate the tertiary transition, which corresponds to a transistion from the amplitude-modulated waves to a three-frequency flow. Of particular interest is that the method also finds a period-doubling bifurcation from the amplitude-modulated rotating waves and a subsequent transition from the flow resulting from this bifurcation.

I. INTRODUCTION

Much can be learned about the fundamental properties of geophysical fluid systems, such as the atmosphere, by studying laboratory experiments that isolate certain key aspects of the system and ignore others that do not determine the essential character of the flow. One

* Contact for G.M. Lewis: Greg.Lewis@ontariotechu.ca

such classical example is the differentially heated rotating fluid annulus experiment [1–5], in which a fluid is placed in a rotating cylindrical annulus while the inner and outer walls of the annulus are held at different temperatures; the flows observed in these experiments resemble those observed in the atmosphere [3]. In many such systems, the fluid flow undergoes a common sequence of transitions upon variation of the system's parameters, e.g. the magnitude of the differential heating and/or the rotation rate [6]. In particular, transitions are observed from axisymmetric flow to rotating waves, then to amplitude-modulated rotating waves (often called amplitude vacillating flow) or other forms of modulated rotating waves, and eventually to irregular flows [3].

Another example of such a system that has geophysical relevance is the sheared annular electroconvection experiment. In this system, a thin liquid crystal film suspended between two annular electrodes is driven to convection by an applied potential difference while a shear is imparted through a rotation of the inner electrode. The system is a close analogue of some laboratory-scale geophysical flow experiments, e.g. those mentioned above [1, 2] (see also [7]), and to simplified models of the rotating equatorial regions of planetary atmospheres and planetary interiors [8, 9]. The radial electrical forces of electroconvection play the role of radial gravity-driven thermal buoyancy in a geophysical context, and all these systems share an $SO(2)$ symmetry. A crucial difference is in the two-dimensional nature of electroconvection. In particular, the electroconvection experiments employ a liquid crystal in smectic A phase, which can essentially be considered as a two-dimensional fluid.

The sheared annular electroconvection experiment exhibits a succession of flow transitions similar to those observed in its geophysical counterparts. In particular, laboratory and numerical studies of sheared annular electroconvection [10–17] have observed that under small applied electric potential difference, the system exhibits axisymmetric flow in which the velocity of the fluid is in the azimuthal direction and the electric current is carried only by conduction between the annular electrodes, while the surface charge remains undisturbed by the flow. At a critical potential difference, a primary transition occurs to rotating waves in which the charge is also convected by the flow, increasing the total current beyond that of pure conduction. Beyond this critical potential difference, it is observed that transitions from the rotating wave state to modulated rotating waves [14], to localized vortices [15], and subsequently to unsteady turbulent flow [16, 17], are observed. As such, in addition to being an ideal system in which to study bifurcations in spatiotemporal pattern formation [18], it

is, in particular, an ideal system in which to study transition phenomena of geophysical relevance.

We propose to use numerical bifurcation methods to study flow transitions in such geophysical fluid systems. In particular, numerical continuation can be used to follow the solutions corresponding to the steady axisymmetric flow, rotating waves, and amplitude-modulated rotating waves, as a parameter of the system is varied, and linear stability analysis can be used to determine transitions from these solutions. The application of this approach to a model of sheared annular electroconvection that we present here is an indication of its effectiveness. In relation to numerical experimentation, i.e. using time-stepping simulations alone, such bifurcation techniques are able to compute unstable solutions, and are able to unambiguously and accurately determine the range of parameters over which a flow is stable, even when the ranges are small. Bifurcation methods can also determine regions of bistability without relying on finding specific initial conditions that lead to the different stable solutions. They can determine the type of bifurcation associated with the transition, even in the case of subcritical bifurcations, and can determine the form of the instability leading to the transition. Thus, a clearer picture of the dynamics of the system can be discovered. However, the advantages of this approach are balanced by the increase in the required computational resources in comparison with time-stepping methods alone.

Steady axisymmetric flows correspond to steady solutions of the model equations, while the rotating waves and amplitude-modulated rotating waves correspond to periodic orbits and invariant tori, respectively. Numerical methods have been developed for the parameter continuation of such solutions in large-dimensional systems, with special interest in applications to fluid dynamics; see, e.g. [19] for a review. Some such methods, e.g., [20–22], are based on time-integration of the dynamical system. These methods can be useful, in particular, when a time-stepping (i.e. simulation) code is already available, as is often the case. The method of Tuckerman and Barkley [22] effectively uses the linear part of the time-stepping code as a preconditioner to solve for steady solutions of the model equations; this method, however, cannot be generally used to compute periodic orbits. The approach of Sanchez et al. [20, 21] formulates the solution of the relevant flows as fixed points of maps, and can be used to compute steady solutions and periodic orbits, and can be extended for the computation of invariant tori.

In many geophysical systems, it is possible to use the rotational property of the flow to aid

in the reduction of the computational cost. In particular, our approach uses the observation that the rotating waves are relative equilibria with respect to a rotating reference frame. Consequently, the rotating waves can be computed as steady solutions with an additional unknown, corresponding to the constant phase speed of the rotating wave. This approach has been used extensively in the context of fluid dynamics; see, e.g., [19, 23–26]. Not common is the application to amplitude-modulated rotating waves, which are periodic orbits when viewed in an appropriately defined rotating reference frame [6]. This idea has been used by [27] to compute such solutions in thermal convection in a spherical shell. We use a similar approach here. In particular, we use a Newton-Krylov method based on time-integration, in a formulation in which the rotating waves and modulated rotating waves are computed as fixed points of a discrete dynamical system (a map) [20]. Stability of the flows can be determined in terms of the stability of the fixed points of the map. Here, unlike [27], we do not use an explicit implementation of the discretized linearized equations in the computations, but instead use a finite-difference approximation of the action of the linearized map. This requires the use of a different auxiliary condition than that of [27] for the defining system used in the numerical continuation of the modulated rotating waves. In particular, the advantage of our approach is that the numerical simulation code is only required to act as a 'black-box', i.e. it can be used directly without modification, which significantly simplifies the implementation. In addition, unlike [27], our computations, at least in the application to the electroconvection problem, require the use of preconditioning (see [20, 28] and Section IV C). Although, here, we present an application of the numerical method to the electroconvection problem, the method can be applied in a straightforward manner for the continuation of rotating waves and amplitude-modulated rotating waves in other applications.

In Section II, we provide details of the electroconvection experiment and of the mathematical and numerical models used in the study. In Section IV, we introduce the methods, and discuss some details of the implementation. The results and discussion are presented in Section V.

II. ELECTROCONVECTION

Electroconvection refers to fluid flows generated by electrical forces acting on space charges within the fluid, or on surface charges at the interfaces between fluids [29]. Here, we will be concerned with convection of thin liquid films driven by surface charges. Smectic A liquid crystals are layered materials that naturally form stable suspended films composed of weakly conducting organic liquids. In the smectic A phase, the elongated molecules arrange themselves into layers with their long axes oriented perpendicular to the layers. A layer is of nano-meter thickness and, within a layer, the oriented molecules move freely as in a normal Newtonian viscous liquid, while molecular motion between layers is very restricted, as in a soft solid. A suspended smectic A film has a submicron film thickness and consists of an integer number of discrete molecular layers that move together as a nearly ideal 2-D fluid and strongly resist variations in the film thickness. When suspended between electrodes, the films readily form surface charges that interact with the electric field to produce flow; the film can span a distance between electrodes on the order of millimeters.

Many laboratory experiments on electroconvecting smectic A films, using various geometries, have been reported, including rectangular geometry [30–33], annular geometry [13], and annular films with an applied shear [10–12, 34]; see also [35]. Here, we consider the experiment of Tsai et al. [12] which employs a smectic A film suspended between two concentric annular electrodes. The inner electrode is rotated at a constant angular speed ω_i, imposing a radial shear, and a DC voltage V is applied between the two electrodes. See Figure 1. The working fluid is 8CB (4-cyano-4'octylbiphenyl) [12], which is in the smectic A phase at room temperature.

The standard experimental protocol of Tsai et al. [12] consisted of measuring the current I between the electrodes as the applied DC voltage V is incremented from zero to a maximum value in small steps, and then similarly decremented back to zero, with the inner anode rotating at a prescribed constant angular speed ω_i and the outer cathode stationary and grounded. For relatively low voltage, the fluid flow is axisymmetric. In this state, the velocity of the fluid is in the azimuthal direction where the flow lines are concentric circles and the current passes between the electrodes by conduction. However, when the applied voltage V exceeds a critical voltage V_c, the axisymmetry is broken and the fluid becomes arranged into symmetric pairs of convective vortices. At higher voltages, more complicated

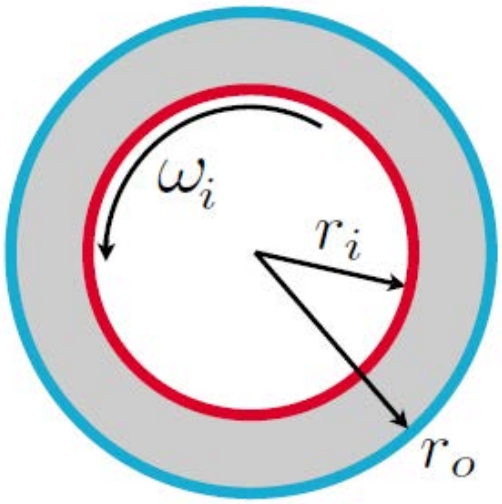

FIG. 1. The geometry of sheared annular electroconvection. The liquid crystal is confined in an annular region $r_i \leq r \leq r_o$, and the inner electrode rotates at a constant rate ω_i.

flows are provoked.

It is shown in [11, 12], that, for various rotation rates ω_i, the primary transition to convection is supercritical, i.e. the amplitude of the observed convective vortices grows monotonically from zero as the applied voltage V increases from V_c. Furthermore, the rotation acts as a stabilizer of the flow, delaying the onset of convection.

These transitions have been reproduced with numerical simulations [14, 17]. The numerical experiments consisted of long-time integrations using a random perturbation from the base state solution (axisymmetric flow) as the initial condition. Simulations were conducted for a wide range of applied voltage V for a fixed rotation rate ω_i. In addition to reproducing the transition from the axisymmetric flow to rotating waves, a secondary transition from rotating waves to amplitude-modulated rotating waves was found.

A. The Mathematical Model

The mathematical model of electroconvection used in this paper is based on the one described in [10]. We start with a summary of this model; for futher details see [10]. In the physical experiment, the thin film is confined in an annular region defined in circular cylindrical coordinates (r, θ, z) as, $r_i \leq r \leq r_o$; see Figure 1. The film is a liquid crystal in

smectic A phase with uniform thickness s, and gap width $d = r_o - r_i$. Since $s \ll d$, the film is treated as a 2D electrically conducting Newtonian fluid lying in the plane $z = 0$. The density, dynamic viscosity and conductivity of the fluid are denoted by ρ, η and σ respectively. The inner electrode, $0 \leq r \leq r_i$, $z = 0$, is rotating at a constant angular speed ω_i and is held at a constant electric potential V. The outer electrode, $r \geq r_o$, $z = 0$, is held at zero potential and does not rotate. The conservation of momentum and the conservation of matter, given by the incompressible Navier-Stokes equations with an electric body force $q\mathbf{E}$, model the velocity field $\mathbf{u}(r, \theta, t) = u(r, \theta, t)\hat{\mathbf{r}} + v(r, \theta, t)\hat{\boldsymbol{\theta}}$, where $\hat{\mathbf{r}}$ is the unit vector in the radial direction, $\hat{\boldsymbol{\theta}}$ is the unit vector in the azimuthal direction, q is the surface charge density, $\mathbf{E} = -(\nabla\psi)|_{z=0}$ is the electric field in the film plane $z = 0$, ∇ is the 2D gradient operator, and ψ is the 3D electric potential which extends both above and below the film [10, eqns (2.1), (2.2)]. The conservation of charge is expressed by a continuity equation where the current density $\mathbf{J}$ is composed of an ohmic conduction term $\sigma\mathbf{E}$, and a convective term $q\mathbf{u}$ due to the fluid motion [10, eqn (2.3)]. The 3D electric potential ψ satisfies the Laplace equation in the charge-free region $z \neq 0$ with a boundary condition that depends on the surface charge density q [10, eqns (2.4) (2.5)].

The system is subject to the following boundary conditions. At each electrode, the velocity field satisfies no-slip boundary conditions

$$\mathbf{u} = \omega_i r_i \hat{\boldsymbol{\theta}}, \qquad r = r_i, \tag{1a}$$

$$\mathbf{u} = \mathbf{0}, \qquad r = r_o. \tag{1b}$$

The potential ψ is set to zero at infinity

$$\lim_{z \to \pm\infty} \psi(r, \theta, z) = 0, \tag{1c}$$

and, at $z = 0$, takes on the imposed voltage, so that

$$\psi(r, \theta, 0) = \psi_2(r, \theta) = \begin{cases} V, & \text{for } r \leq r_i, \\ 0, & \text{for } r \geq r_o, \end{cases} \tag{1d}$$

where ψ_2 is the 2D electric potential in the $z = 0$ plane.

A stream function/vorticity formulation is used, where the stream function $\phi = \phi(r, \theta, t)$ and vorticity $\omega = \omega(r, \theta, t)$ satisfy

$$\mathbf{u} = \nabla\phi \times \hat{\mathbf{z}}, \qquad \nabla \times \mathbf{u} = \omega\hat{\mathbf{z}}. \tag{2}$$

In addition, we define a characteristic length, time and charge. If we let the imposed voltage V denote a representative voltage over a length scale of $d = r_o - r_i$ and a relaxation time $\tau_c = \epsilon_0 d/\sigma$, where σ is the conductivity and ϵ_0 is the permeability of free space, then we obtain the following nondimensionalization

$$r = d\tilde{r}, \qquad \phi = \frac{\sigma d}{\epsilon_0}\tilde{\phi}, \qquad \psi = V\tilde{\psi}, \qquad t = \tau_c\tilde{t}, \qquad q = \frac{\epsilon_0 V}{d}\tilde{q}, \tag{3}$$

where the tilde represents the dimensionless variables. Nondimensionalizing with (3), and dropping the tildes, we obtain the system of equations describing the evolution of the dimensionless physical quantities, i.e. the vorticity ω, stream function ϕ, charge density q, the 2D potential in the fluid ψ_2 and the 3D potential ψ:

$$\nabla^2\phi = -\omega, \tag{4a}$$

$$\frac{\partial\omega}{\partial t} + (\mathbf{u}\cdot\nabla)\,\omega = \mathcal{P}\nabla^2\omega + \mathcal{P}\mathcal{R}\,(\nabla\psi_2 \times \nabla q)\cdot\hat{\mathbf{z}}, \tag{4b}$$

$$\frac{\partial q}{\partial t} + (\mathbf{u}\cdot\nabla)\,q = \nabla^2\psi_2, \tag{4c}$$

$$\left(\nabla^2 + \frac{\partial^2}{\partial z^2}\right)\psi = 0, \qquad q = -2\frac{\partial\psi}{\partial z}\Big|_{z=0^+}, \tag{4d}$$

where the nondimensional parameter groups are defined as

$$\mathcal{R} = \frac{\epsilon_0^2 V^2}{\sigma\eta}, \qquad \mathcal{P} = \frac{\epsilon_0\eta}{\rho\sigma d}. \tag{5}$$

The dimensionless parameter $\mathcal{R}$, which is analogous to the dimensionless Rayleigh number that arises in thermal convection, is proportional to the square of the applied voltage V and describes the relative strength of the applied electric forcing to the viscous dissipation. The dimensionless parameter $\mathcal{P}$ is analogous to the Prandtl number and is a fluid parameter that describes the ratio of the charge relaxation time to the viscous relaxation time. For simplicity, we will refer to $\mathcal{R}$ as the electric Rayleigh number, or simply the Rayleigh number, and $\mathcal{P}$ as the electric Prandtl number, or simply the Prandtl number. However, we will use the script letters to refer to these dimensionless parameters to highlight the differences with their dimensionless counterparts that arise in thermal convection.

The dimensionless boundary conditions are

$$\frac{\partial}{\partial r}\phi(r_o,\theta) = 0, \qquad \phi(r_o,\theta) = 0, \tag{6a}$$

$$\frac{\partial}{\partial r}\phi(r_i,\theta) = -\frac{\omega r_i\epsilon_0}{\sigma} = -\omega_i r_i\tau_c, \qquad \phi(r_i,\theta,t) = g(t), \tag{6b}$$

$$\psi_2(r_i,\theta) = 1, \qquad \psi_2(r_o,\theta) = 0, \tag{6c}$$

$$\psi(r,\theta,0) = \begin{cases} 1, & \text{for } 0 \le r \le r_i, \\ \psi_2(r,\theta), & \text{for } r_i \le r \le r_o, \\ 0, & \text{for } r \ge r_o, \end{cases} \tag{6d}$$

$$\lim_{z\to\pm\infty} \psi(r,\theta,z) = 0, \tag{6e}$$

where $g(t)$, which gives the value of the stream function ϕ on the inner electrode, must be computed (see below). The width of the film in dimensionless units is $r_o - r_i = 1$. The problem does not depend on r_o and r_i separately, rather it depends on the radius ratio $\alpha = r_i/r_o$. Indeed, the dimensionless radii can be expressed as

$$r_i = \frac{\alpha}{1-\alpha}, \qquad\qquad r_o = \frac{1}{1-\alpha}. \tag{7}$$

The experimental studies have radius ratio $\alpha = 0.56$ [10] and $\alpha = 0.8$ [12]. See [10] for a study on how the linear stability of the base state depends on α.

The stream function ϕ is determined up to a (possibly time-dependent) constant, which can be determined with a single additional condition of our choosing. The radial component of the no-slip boundary condition (1a)–(1b) implies that the stream function is independent of θ at the boundaries. Thus, if there were only one boundary, one could choose this undetermined constant using the condition that the stream function be zero at that boundary. As there are two boundaries, we can choose the additional condition to be that the stream function at the *outer* boundary be zero (as indicated in (6a)), but it remains to close the system by determining the stream function at the inner boundary (i.e. the function $g(t)$, see (6b)). We do not have the freedom to determine $g(t)$ using a second condition of our choosing, and therefore it must be determined from the flow. In particular, $g(t)$ is given by the total azimuthal flux, and is determined from the azimuthal component of the velocity as follows:

$$\int_{r_i}^{r_o} v(r,\theta,t)\, dr = \phi(r_i,\theta,t) - \phi(r_o,\theta,t) = g(t) - 0 \quad \Longrightarrow \quad g(t) = \int_{r_i}^{r_o} \widehat{v}_0(r,t)\, dr, \tag{8}$$

where an average in the azimuthal variable θ has been taken, the hat denotes an azimuthally averaged quantity, and $\widehat{v}_0(r,t)$ satisfies the following partial differential equation

$$\frac{\partial \widehat{v}_0}{\partial t} + \left(\widehat{u\frac{\partial v}{\partial r}}\right)_0 + \frac{1}{r}\left(\widehat{uv}\right)_0 = \mathcal{P}\left(\frac{1}{r}\frac{\partial \widehat{v}_0}{\partial r} + \frac{\partial^2 \widehat{v}_0}{\partial r^2} - \frac{1}{r^2}\widehat{v}_0\right) - \frac{\mathcal{P}\,\mathcal{R}}{r}\left(\widehat{q\frac{\partial \psi_2}{\partial \theta}}\right)_0, \tag{9}$$

which is found by computing the azimuthal average of the azimuthal component of the incompressible Navier-Stokes equations with an electric body force [10, eqns (2.1), (2.2)]. Integrating (9) with respect to r yields an ODE for $g(t)$, closing the system

$$\frac{dg}{dt} = \int_{r_i}^{r_o} \left[\mathcal{P} \left(\frac{1}{r}\frac{\partial \widehat{v}_0}{\partial r} + \frac{\partial^2 \widehat{v}_0}{\partial r^2} - \frac{1}{r^2}\widehat{v}_0 \right) - \frac{\mathcal{P}\,\mathcal{R}}{r} \left(q \widehat{\frac{\partial \psi_2}{\partial \theta}} \right)_0 - \left(\widehat{u\frac{\partial v}{\partial r}} \right)_0 - \frac{1}{r} \left(\widehat{uv} \right)_0 \right] dr. \quad (10)$$

The PDEs (4a)–(4d), (10) with the boundary conditions (6a)–(6e) describe both sheared and unsheared annular electroconvection. We note that, unlike in [10], no approximation has been made for the stream function at the inner electrode. In that work, the authors made the approximation of $\phi(r_i, \theta, t) = 0$, and so no equation like (10) was needed to close the system.

1. *The deviation equations*

The rotation of the inner electrode generates an axisymmetric steady Couette shear, which is observed at low $\mathcal{R}$. This flow is characterized by a dimensionless Reynolds number

$$Re = \frac{r_i \Omega}{\mathcal{P}}, \quad (11)$$

where $\Omega = \tau_c \omega_i$ is the dimensionless angular frequency of the inner electrode. We call this flow the base state, and denote it by a superscript zero. This flow can be computed analytically by considering only steady axisymmetric solutions of (4a)–(4d) with boundary conditions (6a)–(6e). In particular, the base state is given by

$$\frac{\partial \phi^{(0)}(r)}{\partial r} = Re\,\mathcal{P} \frac{r_i}{r_o^2 - r_i^2} \left(r - \frac{r_o^2}{r} \right), \quad (12a)$$

$$\omega^0(r) = -2\,Re\,\mathcal{P} \left(\frac{r_i}{r_0^2 - r_i^2} \right), \quad (12b)$$

$$q^{(0)}(r) = \frac{2}{\ln(r_i/r_o)} \left(\frac{1}{r_o} F\left(\frac{1}{2}, \frac{1}{2}; 1; \frac{r^2}{r_o^2} \right) - \frac{1}{r} F\left(\frac{1}{2}, \frac{1}{2}; 1; \frac{r_i^2}{r_o^2} \right) \right), \quad (12c)$$

$$\psi_2^{(0)}(r) = \begin{cases} 1, & \text{for } 0 \le r \le r_i, \\ \frac{\ln(r/r_o)}{\ln(r_i/r_o)}, & \text{for } r_i \le r \le r_o, \\ 0, & \text{for } r \ge r_o, \end{cases} \quad (12d)$$

$$\psi^{(0)}(r, z) = \int_0^\infty A(k) J_0(kr) e^{-kz} \mathrm{d}k, \quad (12e)$$

see [10], where F is a hypergeometric function, J_0 is the zeroth Bessel function and

$$A(k) = k \int_0^\infty \psi^{(0)}(r,0) J_0(kr) r \mathrm{d}r. \tag{13}$$

Equation (12a) can be integrated from r_i to r_o to obtain an explicit form for $\phi^{(0)}$ that satisfies the boundary condition (6b) with

$$g(t) = g^{(0)} = Re\,\mathcal{P}\left(\frac{r_i}{2} - \frac{r_i r_o^2}{r_o^2 - r_i^2}\ln\left(\frac{r_o}{r_i}\right)\right). \tag{14}$$

We note that, in this experiment, the inner electrode is rotating at a constant rate while the outer electrode is fixed. However, independent rotations of the electrodes can be dealt with by applying a transformation to a rotating frame of reference, where the outer electrode is stationary. The Coriolis forces introduced by the transformation can be absorbed into the pressure term of the corresponding Navier-Stokes equations.

We can write the dependent variables in terms of their deviations from the base state:

$$q(r,\theta,t) = q^{(0)}(r) + q^{(1)}(r,\theta,t), \tag{15}$$

and likewise for the other dependent variables, where the deviations are identified using a superscript 1, e.g. $q^{(1)}$. It is convenient to rewrite the equations (4c)–(4d) in terms of the deviations, $\phi^{(1)}$, $\psi^{(1)}$ and $q^{(1)}$, instead of their counterparts, ϕ, ψ and q, respectively. Upon applying this decomposition and substituting into (4c)–(4d), we obtain equations which govern the evolution of the charge density deviation $q^{(1)}$ and the potential deviation $\psi^{(1)}$:

$$\frac{\partial q^{(1)}}{\partial t} + \frac{1}{r}\left(\frac{\partial q^{(0)}}{\partial r}\frac{\partial \phi^{(1)}}{\partial \theta} + \frac{\partial q^{(1)}}{\partial r}\frac{\partial \phi^{(1)}}{\partial \theta} - \frac{\partial \phi^{(0)}}{\partial r}\frac{\partial q^{(1)}}{\partial \theta} - \frac{\partial \phi^{(1)}}{\partial r}\frac{\partial q^{(1)}}{\partial \theta}\right) - \nabla^2 \psi_2^{(1)} = 0, \tag{16a}$$

$$\left(\nabla^2 + \frac{\partial^2}{\partial z^2}\right)\psi^{(1)} = 0, \qquad q^{(1)} = -2\frac{\partial \psi^{(1)}}{\partial z}\Big|_{z=0}. \tag{16b}$$

The deviation variables, $\psi_2^{(1)}$ and $\psi^{(1)}$, satisfy the following boundary conditions

$$\psi_2^{(1)}(r_i,\theta) = \psi_2^{(1)}(r_o,\theta) = 0, \tag{17a}$$

$$\psi^{(1)}(r,\theta,0) = \begin{cases} 0, & \text{for } 0 \le r \le r_i, \\ \psi_2^{(1)}(r,\theta), & \text{for } r_i \le r \le r_o, \\ 0, & \text{for } r \ge r_o, \end{cases} \tag{17b}$$

$$\lim_{z\to\pm\infty} \psi^{(1)}(r,\theta,z) = 0. \tag{17c}$$

Thus, equations (4a)–(4b), (10), (16a)–(16b) with boundary conditions (6a)–(6b), (17a)–(17c) form a closed set of equations describing both sheared and unsheared annular electroconvection.

III. THE NUMERICAL TIME-STEPPER

In this section, we provide a brief overview of the pseudo-spectral time-stepper for the PDEs (4a)–(4b), (10), (16a)–(16b) with boundary conditions (6a)–(6b), (17a)–(17c). The time-stepper is implemented in MATLAB and is, in many ways, very similar to that described in [14, 17]. The 2D physical quantities, the stream function ϕ, the vorticity ω, the charge density deviation $q^{(1)}$ and the electric potential deviation $\psi_2^{(1)}$, are approximated using a truncated Fourier series $\{e^{im\theta}\}$ in the $\hat{\boldsymbol{\theta}}$ direction and a truncated Chebyshev series $\{T_n(r)\}$ in the $\hat{\mathbf{r}}$ direction. That is, we write

$$\phi(r,\theta,t) = \sum_{n=0}^{N_c} \sum_{m=-K}^{K} \tilde{\phi}_{nm}(t) e^{im\theta}\, T_n(x), \tag{18}$$

and similarly for the other physical quantities, where K is the highest Fourier mode, N_c is the order of the highest Chebyshev polynomial, and

$$x = 2\frac{r - r_i}{r_o - r_i} - 1 \tag{19}$$

linearly maps $r \in [r_i, r_o]$ to $x \in [-1, 1]$.

The AB/BDI2 time-stepping scheme

$$\frac{3\mathbf{u}^{(k+1)} - 4\mathbf{u}^{(k)} + \mathbf{u}^{(k-1)}}{2\delta t} \approx \frac{\partial \mathbf{u}}{\partial t} = \mathcal{L}(\mathbf{u}) + \mathcal{N} \approx \mathcal{L}(\mathbf{u}^{(k+1)}) + 2\mathcal{N}^{(k)} - \mathcal{N}^{(k-1)}, \tag{20}$$

is implemented, where δt is a prescribed time step and $\mathbf{u}^{(k)}$ is the spatially discretized solution vector at the kth time-step (see e.g. [36]). This scheme is a second-order implicit-explicit method, in which the nonlinear part $\mathcal{N}$ is treated explicitly and the linear part $\mathcal{L}(u)$ is treated fully implicitly. It has also been referred to as SBDF (semi-implicit BDF) and as extrapolated Gear [37, 38].

The charge density deviation $q^{(1)}$ and the potential deviation $\psi_2^{(1)}$ are nonlocally related to one another via the three-dimensional Laplace equation (16b). Rather than computing this three-dimensional elliptic problem, $q^{(1)}$ can be computed directly from $\psi_2^{(1)}$ using a Dirichlet-to-Neumann map. Similarly, the stream function ϕ and the vorticity ω are nonlocally related

via the vorticity equation (4a) and one can be recovered from the other using a linear map. The time-stepper proceeds as follows: the potential deviation $\psi_2^{(1)}$ and the vorticity ω are advanced by one time step, after which the charge deviation $q^{(1)}$ and the stream function ϕ are computed at this new time using the newly-computed potential deviation and vorticity, respectively. The Orszag 3/2 aliasing rule is performed when constructing the nonlinear terms needed for (20). With appropriately chosen starting values, the method is second-order accurate in time.

For more details on the time-stepper, the reader is referred to [14, 17]. The method we use is essentially the same, except that in those works the authors time-step the stream function deviation $\phi^{(1)}$ and the vorticity deviation $\omega^{(1)}$, while we time-step the stream function ϕ and the vorticity ω. Also in [14, 17], as in [10], the approximation that $\phi^{(1)}(r_o, t) = \phi^{(1)}(r_i, t) = 0$ is made [39]. We do not make this approximation, and, therefore, we need to time-step (10), starting from (8), for the full stream function ϕ. Specifically, from (8), $g(t)$ is the radial integral of $\widehat{v}_0(r, t)$. We time-step (9) to find $\widehat{v}_0^{(k+1)}$, where, here, the superscript denotes the $k+1$st time-step, and then use Chebyshev-Gauss quadrature to approximate the radial integral, thus determining $g^{(k+1)}$. The time-stepping is done as follows. First, the velocity components $u^{(k-1)}$, $u^{(k)}$, $v^{(k-1)}$, and $v^{(k)}$ are determined from the stream function $\phi^{(k-1)}$ and $\phi^{(k)}$. The nonlinear terms $u\frac{\partial v}{\partial r}$, uv, and $q\frac{\partial \psi_2}{\partial \theta}$ are computed at the $(k-1)$st and kth time levels. Applying the Fast Fourier Transform (FFT) and then selecting the component that approximates the zeroth Fourier coefficient determines the nonlinear terms of (9): $\widehat{\mathcal{N}^{(k-1)}}_0$ and $\widehat{\mathcal{N}^{(k)}}_0$. The time-stepping (20) is then applied to (9), determining $\widehat{v}_0^{(k+1)}$.

A two-step method, such as (20), requires two initial values. One initial value, at $t = 0$, is given by the initial conditions of the problem. A second initial value, at $t = \delta t$, must be provided by some other mechanism. It is common to simply take one step, of size δt, with a lower-order one-step method to generate this second initial value. In the context of the bifurcation methods discussed in IV, which are built upon time-integration methods using the time-stepper, this approach may not provide sufficient accuracy. Specifically, if the "$t = 0$" initial value is on the periodic solution at $t = 0$, to a given tolerance, then the "$t = \delta t$" initial value also needs to be on the periodic solution at $t = \delta t$, to a similar tolerance, otherwise the method may not converge to the desired solutions; this is particularly important when considering unstable solutions. Thus, unlike in the application of the time-stepper as discussed in [14, 17], here, it is vital that the second initial condition

be sufficiently accurate. To this end, we use a hierarchy of discretizations to produce a more accurate approximation of the solution at time $t = \delta t$. Specifically, a one-step first-order scheme is used with a very small time-step, e.g. $\delta t/k$, where k is some integer, to generate an approximation of the solution at $t = \delta t/k$. This approximation is used as the second initial condition for the two-step method, using a time-step of $\delta t/k$, to obtain an approximation at $t = n\delta t/k$. This approximation is subsequently used as the second initial step for the two-step method with time-step $n\delta t/k$, where n is some integer. This is then repeated, with sequentially increasing step size, to generate an approximation of the solution at $t = \delta t$. Once the two required initial values at $t = 0$ and $t = \delta t$ are available, the time-stepper can then be used with time step δt for the rest of the computation. Here, we use $n = 5$ and $k = n^5$.

IV. METHODS FOR COMPUTING SPECIAL SOLUTIONS

After spatial discretization using the spectral methods described above, our model can be written as a continuous dynamical system in the general form

$$\mathcal{M}\frac{\mathrm{d}\mathbf{u}}{\mathrm{d}t} = \mathbf{F}(\mathbf{u}, \mu), \qquad \mathbf{F} : \mathbb{R}^n \times \mathbb{R} \to \mathbb{R}^n, \tag{21}$$

where $\mathbf{u} = \mathbf{u}(t) \in \mathbb{R}^n$ is the discretized solution vector, μ is a real parameter, and the matrix $\mathcal{M}$ may not be invertible due to algebraic constraints. Here, μ is the Rayleigh number $\mathcal{R}$ and the solution vector $\mathbf{u}$ contains the four physical quantities (the electric potential deviation $\psi_2^{(1)}$, the charge density deviation $q^{(1)}$, the vorticity ω, and the stream function ϕ), and has size $n = 4(2K + 1)(N_c + 1)$, where K is the highest Fourier mode and N_c is the highest degree of Chebyshev polynomial as shown in Section III.

A. Computation of rotating waves

The solutions of the continuous dynamical system (21) corresponding to rotating waves can be computed as fixed points of a flow map Φ_t:

$$\mathbf{u} \to \Phi_t(\mathbf{u}, \mu), \qquad \Phi_t : \mathbb{R}^n \times \mathbb{R} \times \mathbb{R} \to \mathbb{R}^n, \tag{22}$$

which maps an initial condition $\mathbf{u} \in \mathbb{R}^n$ to the solution of (21) at time $t \in \mathbb{R}$, for a fixed parameter $\mu \in \mathbb{R}$. In particular, the rotating waves are limit cycles, and thus, such solutions

of (21) must satisfy $\mathbf{u}(t) = \mathbf{u}(t+\tau_w)$, where τ_w is the period of the limit cycle. Therefore, the flow map $\Phi_{\tau_w}(\mathbf{u}, \mu)$ will map $\mathbf{u}$ to itself, for any $\mathbf{u}$ on the limit cycle, and thus the rotating waves can be found as fixed points of the map Φ_{τ_w} by solving

$$\Phi_{\tau_w}(\mathbf{u}, \mu) - \mathbf{u} = 0, \tag{23}$$

where τ_w is to be determined. This method, however, requires each integration of the map to be over a full period τ_w, and therefore, we choose, instead, a less general, but more efficient, approach. In particular, we use the property that the rotating waves are relative equilibria, i.e., integration through any time t is equivalent to rotation by $\tilde{\theta} = wt$, where w is the constant phase speed of the wave. Therefore, all points $\mathbf{u}$ on the rotating wave must satisfy

$$\Phi_t(\mathbf{u}, \mu) - \gamma\mathbf{u} = 0, \tag{24}$$

where the rotation operator $\gamma \in SO(2)$ acts on $\mathbf{u}$ via $\gamma\mathbf{u} = \mathbf{u}(r, \theta - wt)$, the phase speed w is to be determined, and t is arbitrary and thus may be taken to be much smaller than the period τ_w.

Equation (24) defines the rotating wave up to a phase, and therefore, to obtain uniqueness, we introduce the phase condition

$$\frac{\partial}{\partial\theta}\mathbf{u}^{(0)} \cdot \left(\mathbf{u} - \mathbf{u}^{(0)}\right) = 0, \tag{25}$$

which chooses the phase relative to a reference solution $\mathbf{u}^{(0)}$, usually chosen to be the initial guess used for the nonlinear solver (see below). The phase condition ensures that we seek corrections to $\mathbf{u}^{(0)}$ that are orthogonal to the tangent to the symmetry generator $\frac{\partial}{\partial\theta}\mathbf{u}^{(0)}$, the derivative of $\mathbf{u}^{(0)}$ with respect to θ. We choose to seek corrections orthogonal to $\mathbf{u}^{(0)}$ instead of $\mathbf{u}$ to remove the complication of working with an extra nonlinear equation.

The nonlinear system given by (24) and (25) can then be solved using Newton's method, in which case updates $\left[\delta\mathbf{u}_j^{(k)}, \delta w_j^{(k)}\right]$ at each iteration k are found from the linear system

$$\begin{bmatrix} \mathrm{D}_{\mathbf{u}}\Phi_t(\mathbf{u}_j^{(k)}, \mu_j) - \gamma & t\frac{\partial \mathbf{u}_j^{(k)}}{\partial\theta} \\ \frac{\partial \mathbf{u}^{(0)}}{\partial\theta} & 0 \end{bmatrix} \begin{bmatrix} \delta\mathbf{u}_j^{(k)} \\ \delta w_j^{(k)} \end{bmatrix} = \begin{bmatrix} \mathbf{u}_j^{(k)} - \Phi_t(\mathbf{u}_j^{(k)}, \mu_j) \\ \frac{\partial \mathbf{u}^{(0)}}{\partial\theta} \cdot \left(\mathbf{u}_j^{(k)} - \mathbf{u}^{(0)}\right) \end{bmatrix}, \tag{26a}$$

$$\mathbf{u}_j^{(k+1)} = \mathbf{u}_j^{(k)} + \delta\mathbf{u}_j^{(k)}, \tag{26b}$$

$$w_j^{(k+1)} = w_j^{(k)} + \delta w_j^{(k)}, \tag{26c}$$

where the subscript j labels points along the solution curve Γ, and $\mathrm{D}_{\mathbf{u}}\Phi_t$ is the Jacobian of the map Φ_t. The matrix in the linear system (26a) is of size $(n+1)\times(n+1)$, that is, it is only a single row and column larger than the matrices required for the numerical integration, but it is dense and computationally intensive to compute. However, the action of the Jacobian $\mathrm{D}_{\mathbf{u}}\Phi_t$ on a vector $\delta\mathbf{u}$ can be found from the evolution of an initial perturbation $\delta\mathbf{u}$ as determined by the model equations linearized about the solution $\mathbf{u}$. Thus, if GMRES [40], or some other iterative method, is used to solve the linear system (26a), it is not necessary to form the Jacobian explicitly, because such methods only require knowledge of matrix-vector products involving the Jacobian. As such, each iteration of the linear solve involves a time-integration of the linearized model equations (i.e. the solution of a variational problem).

If code for the linearization is not available, the action of $\mathrm{D}_{\mathbf{u}}\Phi_t$ on $\delta\mathbf{u}$ can be approximated using a finite-difference method, e.g., the forward finite-difference approximation can be used

$$\mathrm{D}_{\mathbf{u}}\Phi_t(\mathbf{u},\mu)\delta\mathbf{u} \approx \frac{\Phi_t(\mathbf{u}+\epsilon\delta\mathbf{u},\mu)-\Phi_t(\mathbf{u},\mu)}{\epsilon}, \tag{27}$$

for some $\epsilon > 0$. Thus, the action of $\mathrm{D}_{\mathbf{u}}\Phi_t$ on the vector $\delta\mathbf{u}$ can be approximated given knowledge of the action of Φ_t on the vectors $(\mathbf{u}+\epsilon\delta\mathbf{u})$ and $\mathbf{u}$. That is, using the approximation (27), each matrix-vector product in the linear solve can be computed from two evaluations of Φ_t. However, one of the two are the same for each GMRES iteration, and therefore, only a single time integration is required per iteration. In general, in order to ensure convergence of the solution of the linear system in a reasonable number of iterations, preconditioning may be required (see, e.g., [28]). We discuss this in Section IV C. When using spectral methods, as we do here, the computation of the derivative with respect to the angle θ and the action of the rotation operator γ on the vector $\delta\mathbf{u}$ can be computed in spectral space as an element-wise multiplication using the Fast Fourier Transform (FFT). As such, these do not contribute significantly to the overall computation time.

These systems can be adapted very simply to incorporate pseudo-arclength continuation [19]. However, we choose to implement natural continuation as we do not observe any limit points along the solution branches.

B. Computation of amplitude-modulated waves

Amplitude-modulated rotating waves correspond to invariant 2-tori in phase space, and resemble rotating waves with the exception that their amplitude varies periodically in time. As such, we can use an extended version of the approach used to compute the rotating waves. In particular, we replace integration for arbitrary time t with integration for time τ the unknown period of the oscillation of the wave amplitude. That is, an amplitude-modulated rotating wave has the property that integration for time τ will be equivalent to rotation by angle $w\tau$ [6]. In this case, there are two unknown parameters, namely, the phase speed w and the unknown period τ of the amplitude, while there are also two phases that need to be specified, namely, the phase of the wave, and the phase of the amplitude oscillation. To fix the phase of the wave, we use the criterion (25) as we did for the rotating waves, while to fix the phase of the amplitude, we consider only corrections to our initial guess that are orthogonal to the initial guess (28c); essentially this selects an amplitude of the solution. Other possibilities exist for this second condition; see [27]. As such, the amplitude-modulated rotating waves can be found from the defining system:

$$\Phi_\tau(\mathbf{u},\mu) - \gamma\mathbf{u} = 0, \tag{28a}$$

$$\frac{\partial}{\partial\theta}\mathbf{u}^{(\mathbf{0})} \cdot \left(\mathbf{u} - \mathbf{u}^{(0)}\right) = 0, \tag{28b}$$

$$\mathbf{u}^{(\mathbf{0})} \cdot \left(\mathbf{u} - \mathbf{u}^{(0)}\right) = 0, \tag{28c}$$

where τ is the (unknown) period of the amplitude oscillations, $\gamma\mathbf{u} = \mathbf{u}(r, \theta - w\tau, \tau)$, w is the phase speed. The phase speed itself does not need to be constant; in particular, we can interpret w as a mean phase speed for which $\tilde{\theta} = w\tau$ gives the angle of rotation required for (28a) to be satisfied.

This system is solved using the same approach as used for the rotating waves. In particular, the linear system to be solved for each Newton iteration is similar to that for the rotating wave (26), and is solved with GMRES, using (27) to approximate the action of the Jacobian $\mathrm{D}_{\mathbf{u}}\Phi$. The linear system contains only a single extra equation, i.e. the amplitude phase equation (28c), and the Jacobian $\mathrm{D}_{\mathbf{u}}\Phi$ is the same size as in (26). Generally, the period τ is much longer than the arbitrarily chosen t, and therefore, the computation of the amplitude-modulated waves requires significantly more computation time, but is not more memory-intensive.

C. Preconditioning

As described above, the linear systems for the Newton iterations can be solved with GMRES. If the spectrum of the matrix associated with the linear system is well clustered, then it may not be necessary to introduce preconditioning to obtain convergence in a reasonable number of the GMRES iterations. See [28] for a general discussion on preconditioning. Generally, for dissipative systems, the spectrum of the Jacobian $\mathrm{D}_{\mathbf{u}}\Phi_t$ is expected to become more clustered around the origin as the integration time t increases, because most of the eigenvalues correspond to stable manifolds of the associated time-dependent problem, and so, the longer the integration time t, the more the map Φ_t will contract the corresponding perturbations. Thus, for sufficiently long integration times, preconditioning may not be required [20]. However, for the current application, we find that even for relatively long integration times, a prohibitively large number of GMRES iterations is required to achieve convergence, and thus preconditioning is required.

The primary reason for considering an iterative method for the solution of the linear systems is not for memory or computational efficiency, but rather because we can compute matrix-vector products involving the Jacobian matrix $\mathrm{D}_{\mathbf{u}}\Phi_t$, even though we do not have an explicit form of $\mathrm{D}_{\mathbf{u}}\Phi_t$. However, for a particular $\mathbf{u}_j^{(k)}$ and μ_j, it is possible to construct the full matrix $\mathrm{D}_{\mathbf{u}}\Phi_t(\mathbf{u}_j^{(k)}, \mu_j)$, column by column, using only matrix-vector products. In particular, the ith column of $\mathrm{D}_{\mathbf{u}}\Phi_t$ is given by the matrix-vector product $[\mathrm{D}_{\mathbf{u}}\Phi_t]\,\mathbf{e}_i$, where $\mathbf{e}_i$ is the ith standard basis vector. Thus, theoretically, an alternative approach could use a direct method for solving the linear systems involving this explicitly constructed matrix. This approach, however, is not practical, because the construction of an approximation of this matrix, using (27), requires $n+1$ evaluations of Φ_t, and would have to be constructed for each Newton iteration (i.e. for each j and k).

We can, however, use $\mathrm{D}_{\mathbf{u}}\Phi_t(\mathbf{u}_j^{(k)}, \mu_j)$, constructed using a particular $\mathbf{u}_j^{(k)}$ and μ_j, to construct a (left) preconditioner for all Newton iterations over a range of parameter values, i.e., for a range of j and k. In particular, we solve the left preconditioned system $P^{-1}(A\mathbf{x} - \mathbf{b}) = \mathbf{0}$ associated with the Newton iterations (26a), where P is $\mathrm{D}_{\mathbf{u}}\Phi_t(\mathbf{u}_j^{(k)}, \mu_j)$ augmented by an additional row corresponding to each auxillary condition (e.g. (25)) and by an additional column corresponding to the derivatives with respect to each of the additional unknowns (e.g. the phase speed w); see (26a). For the particular $\mathbf{u}_j^{(k)}$ and μ_j used

to construct P, P is an approximation of A, which is the 'perfect' preconditioner (i.e. only a single iteration would be required for convergence), but, we find that P also works well as a preconditioner for a large range of $\mathbf{u}$ and μ. Thus, although expensive to compute initially, the same P can be used for all Newton iterations and over a range of parameters. Furthermore, an accurate approximation of $\mathrm{D}_{\mathbf{u}}\Phi_t$ is not required, and therefore, significant efficiency is obtained by computing it using time steps that are significantly larger than those used in the computation of the solutions themselves (e.g. for the continuation of amplitude-modulated rotating waves, we can use a time step of 5e-4 for the computation of the preconditioner, rather than the 2e-4 that we use for the computation of solutions; the savings is more significant in the computation of the rotating waves, see below). In addition, the computation of $\mathrm{D}_{\mathbf{u}}\Phi_t$ is highly parallelizable, as each of the required $n+1$ evaluations of Φ_t are independent. Also, although $\mathrm{D}_{\mathbf{u}}\Phi_t$ is dense, the required memory is the same order of magnitude as that of the matrices involved in the numerical integration itself, due to the use of spectral methods.

D. Linear stability of special solutions

The steady solutions, which are given by $(\mathbf{u}, \mu)$ and the rotating wave solutions $(\mathbf{u}, w, \mu)$ described above can be computed as fixed points of the flow map $\Phi_t(\mathbf{u}, \mu)$; for the steady solutions, t is arbitrary, while for the rotating waves, t is the period τ_w of the corresponding solution, which can be computed from $w\tau_w = 2\pi/m$, where m is the primary azimuthal wave number observed in the rotating wave. Thus, the stability of the solutions can be determined from the spectrum of $\mathrm{D}_{\mathbf{u}}\Phi_t(\mathbf{u}, \mu)$, the linearization of the flow map $\Phi_t(\mathbf{u}, \mu)$ about the fixed point $\mathbf{u}$. In particular, for maps, a fixed point is said to be *linearly stable* if all eigenvalues of the Jacobian $\mathrm{D}_{\mathbf{u}}\Phi_t(\mathbf{u}, \mu)$ lie in the unit circle of the complex plane, and *unstable* if at least one eigenvalue lies outside the unit circle. Bifurcations of the system occur when an eigenvalue crosses the unit circle as a parameter is varied.

The amplitude-modulated rotating wave solutions $(\mathbf{u}, w, \tau, \mu)$ are fixed points of the map $\gamma^{-1}\Phi_\tau(\mathbf{u}, \mu)$, where τ is the period of the amplitude oscillations. The linear stability of these solutions can be found from the eigenvalues of $\gamma^{-1}\mathrm{D}_{\mathbf{u}}\Phi_\tau(\mathbf{u}, \mu)$.

To determine the linear stability of a fixed point of a map, it is sufficient to find the eigenvalues of largest magnitude. For the efficient computation of these eigenvalues, we

would prefer a method that does not require the explicit formation of $\mathrm{D}_{\mathbf{u}}\Phi_t(\mathbf{u},\mu)$. Thus, we use the Implicitly Restarted Arnoldi Method (IRAM), which is a Krylov subspace method that computes approximations of the eigenvalues of largest magnitude of a matrix using only matrix-vector products [41, 42]. Its implementation together with (27) enables us to efficiently approximate the relevant eigenvalues.

V. RESULTS AND DISCUSSION

We apply the methods described in Section IV to the electroconvection problem. In this context, the Rayleigh number $\mathcal{R}$ is used as the bifurcation parameter μ, and $\mathbf{u}$ contains the stream function deviation $\phi^{(1)}$ and the electric potential deviation $\psi_2^{(1)}$; the charge density deviation and the vorticity deviation can be computed directly from these, and therefore are not necessary to consider as variables of the flow map Φ_t. The relevant physical and numerical parameters used for the computations are presented in Table I. The results are presented in the bifurcation diagram of Figure 2.

A. Axisymmetric flow and the primary transition

For all values of the Rayleigh number, the base state (axisymmetric solution) is given by (12); in terms of the deviations, this solution corresponds to the zero solution. Computation of the eigenvalues of the map $D_{\mathbf{u}=0}\Phi_t$ reveals a primary bifurcation from the base state at a critical Rayleigh number $\mathcal{R}_{c1} = 534.1$; see Figure 2. In particular, at $\mathcal{R}_{c1}$, a supercritical Neimark-Sacker bifurcation of the flow map Φ_t occurs, at which a complex conjugate pair of eigenvalues has modulus 1, and for $\mathcal{R} < \mathcal{R}_{c1}$, all eigenvalues have modulus less than 1 [43]. The bifurcating solutions exist for $\mathcal{R} > \mathcal{R}_{c1}$ and correspond to stable rotating waves with azimuthal wave number six. See Figure 3, in which a snapshot of the rotating wave is plotted; deviations from the base state, as opposed to the full solutions, are plotted to highlight the azimuthal variation of the wave. The wave has constant (positive) phase speed and constant amplitude, i.e. as time evolves, the solution maintains its shape and rotates counter-clockwise at a constant rate. See Supplemental Material [44] for an animation of the stream function deviation $\phi^{(1)}$ corresponding to the rotating wave solution at $\mathcal{R} = 560$. We discuss the parameter continuation of the rotating waves in Section V B.

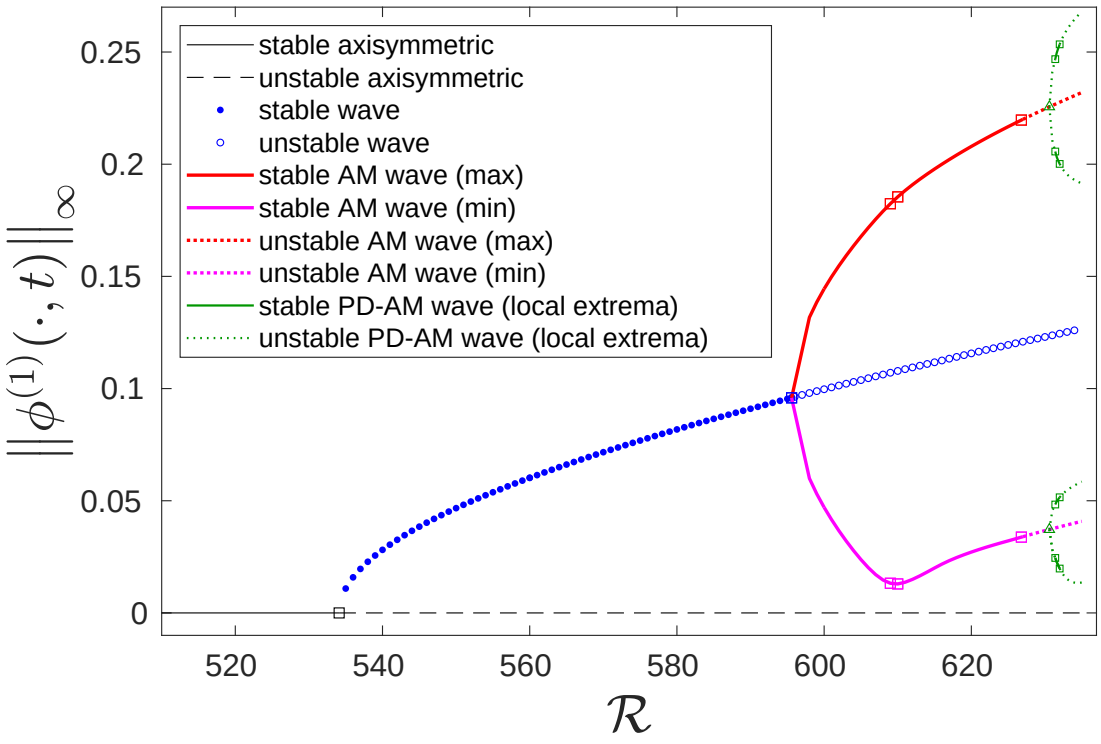

FIG. 2. The bifurcation diagram with Rayleigh number $\mathcal{R}$ as parameter. Solutions are represented in terms of $\left\|\phi^{(1)}(\cdot,t)\right\|_\infty$, the infinity norm of the stream function deviation at a particular time (spatial maximum of $|\phi^{(1)}|$), i.e. the wave amplitude. For the amplitude-modulated (AM) rotating waves, the maximum and minimum amplitude of the solution over a period of the amplitude oscillations is plotted. The squares represent the critical parameter values, i.e. the bifurcation points. The branches labeled PD-AM represent period-2 amplitude-modulated rotating waves resulting from a period-doubling bifurcation (which occurs at the point represented by a triangle); the four PD-AM branches correspond to the two local maxima and two local minima of the wave amplitude that occur over one period of the amplitude oscillation; see Figure 7(b). For a blow-up of this region, and further details, see Figure 8. Values for other parameters are listed in Table I.

The value of t used in the computation of the eigenvalues is arbitrary in the determination of the stability; i.e. although it will affect the eigenvalues, it will not change whether the eigenvalue has modulus greater than or less than 1. We use a value $t = 0.1$, which provides convergence of the Arnoldi method in a reasonable number of iterations. Increasing the value of t increases the separation of the eigenvalues, enabling convergence in fewer iterations, but also increases the cost per iteration. The linear stability is determined from the computation

TABLE I. The parameters used in the numerical results.. RW indicates Rotating Wave. AM indicates Amplitude-Modulated Rotating Wave.

Model parameters		
Symbol	Parameter	Value
$\mathcal{P}$	Prandlt number	75.8
Re	Reynolds number	0.231
α	Aspect ratio	0.56
Time-stepper: discretization parameters		
Symbol	Parameter	Value
N_c	Highest order of the Chebyshev basis	24
K	Highest Fourier wave number	32
δt	Time step (RW/AM)	1×10^{-4} / 2×10^{-4}
δt_P	Time step for preconditioner calculation (RW/AM)	1×10^{-3} / 5×10^{-4}
Numerical bifurcation parameters		
Symbol	Parameter	Value
t	Arbitrary integration time (RW)	0.1
ϵ	Perturbation amplitude of the forward finite difference approximation	10^{-4}
`New_tol`	Newton residual tolerance:	10^{-8}
`gmres_tol`	GMRES tolerance	10^{-6}

of the eigenvalues with the 20 largest magnitudes, using the IRAM MATLAB implementation `eigs`, and the critical value $\mathcal{R}_{c1}$ is computed to a tolerance of 10^{-2} using a secant method. Other parameters are held fixed at the values listed in Table I.

As an accuracy check, the eigenvalues at $\mathcal{R} = 530$ are also computed using a grid size reduced by a factor of two (i.e. using $N_c = 48$ and $K = 64$, see Table I); results are presented in Table II. The reduction in grid size results in differences of at most 0.001, or less than 0.2%, in both the real and imaginary parts. Similarly, the critical Rayleigh number with corresponding critical eigenvalue has been computed on the finer grid; see Table III. The

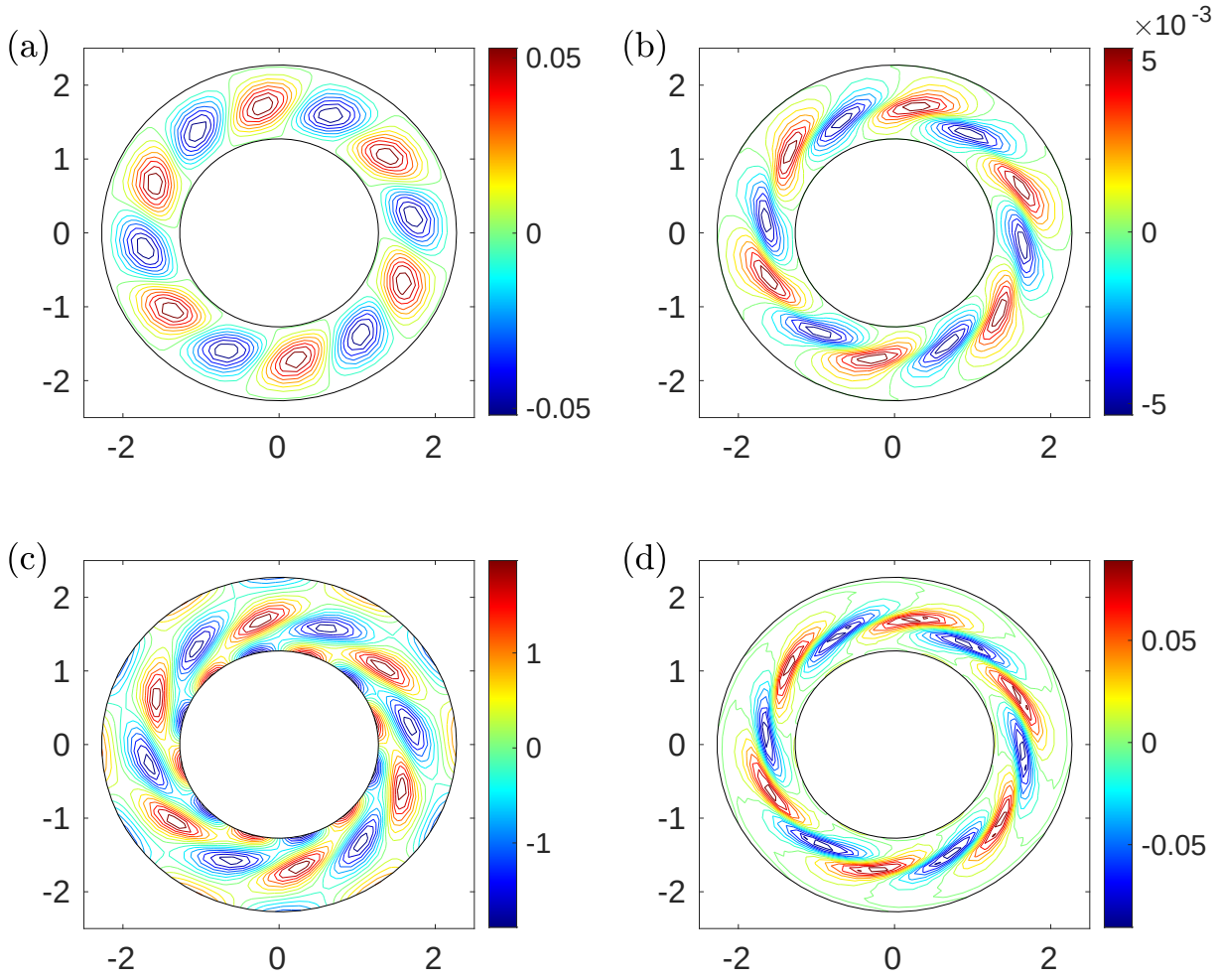

FIG. 3. Rotating wave solution at Rayleigh number $\mathcal{R} = 560$. A snapshot of the deviations from the base state of the four physical quantities are shown: (a) the stream function deviation $\phi^{(1)}$; (b) the 2D electric potential deviation $\psi_2^{(1)}$; (c) the vorticity deviation $\omega^{(1)}$; and (d) the charge distribution deviation $q^{(1)}$. The solution maintains this shape and rotates counter-clockwise at a constant phase speed; see Supplemental Material [44] for an animation of the stream function deviation $\phi^{(1)}$ at $\mathcal{R} = 560$.

critical Rayleigh number on the finer grid differs by less than 0.04, or less than 0.01%.

B. Rotating waves and the secondary transition

The rotating wave solutions, observed for $\mathcal{R} > \mathcal{R}_{c1}$, satisfy (24)–(25), while their linear stability can be determined from the spectrum of $D_{\mathbf{u}}\Phi_{\tau_w}$, where $\tau_w = 2\pi/(mw)$ is the period

TABLE II. Eigenvalues computed with two different grid sizes (N_c, K).

Rayleigh Number $\mathcal{R} = 530$					
(N_c, K)	λ_1, λ_2	λ_3, λ_4	λ_5, λ_6	λ_7	λ_8, λ_9
$(24, 32)$	$0.9425 \pm i0.2098$	$0.2716 \pm i0.8264$	$0.5324 \pm i0.5170$	0.6683	$-0.4258 \pm i0.4662$
$(48, 64)$	$0.9427 \pm i0.2101$	$0.2716 \pm i0.8265$	$0.5320 \pm i0.5181$	0.6683	$-0.4259 \pm i0.4663$
Rayleigh Number $\mathcal{R} = 590$					
(N_c, K)	λ_0	λ_1, λ_2	λ_3	λ_4, λ_5	λ_6, λ_7
$(24, 32)$	1.0000	$0.6551 \pm i0.7131$	-0.9286	$-0.4695 \pm i0.7987$	$0.4503 \pm i0.8200$
$(48, 64)$	1.0001	$0.6622 \pm i0.7124$	-0.9293	$-0.4696 \pm i0.7996$	$0.4504 \pm i0.8202$
Rayleigh Number $\mathcal{R} = 629$					
(N_c, K)	λ_0^a	λ_0^b	λ_1, λ_2	λ_3	λ_4, λ_5
$(24, 32)$	1.0000	1.0007	$0.1286 \pm i1.0249$	-0.9509	$0.4082 \pm i0.2911$
$(48, 64)$	0.9999	1.0006	$0.1296 \pm i0.9846$	-0.9209	$0.3818 \pm i0.2918$

of the rotating wave, and w and m are its phase speed and primary azimuthal wave number, respectively. As we continue the rotating wave solution in the Rayleigh number $\mathcal{R}$, the amplitude of the rotating wave grows from zero at $\mathcal{R} = \mathcal{R}_{c1}$ as shown in Figure 2, while the phase speed w does not vary significantly along the branch; specifically, the phase speed w decreases monotonically from 5.06 at $\mathcal{R} = \mathcal{R}_{c1}$ to 5.05 at $\mathcal{R} = 630$.

Each point on the rotating wave solution branch $\{(\mathbf{u}_j, w_j, \mathcal{R}_j)\}$ is obtained by using the Newton solver to correct an initial guess to within the desired residual tolerance of 10^{-8} in the infinity norm. The initial guess is obtained by following a secant to the branch which is computed from the two previous (known) points on the branch. The initial guess for the first two points on the branch is obtained by time stepping a random initial condition for $t = 10$, with $\mathcal{R} = 560$ and 561. At this parameter value the solution associated with the flow of rotating waves is stable and the time integration produces a sufficiently good guess to obtain convergence of the Newton iterations. Along the solution branch, convergence in approximately three Newton iterations is obtained when the parameter is incremented by

TABLE III. Critical Rayleigh Number $\mathcal{R}_c$ and corresponding eigenvalues; numerical values computed with two different grid sizes (N_c, K).

Primary Transition

(N_c, K)	$\mathcal{R}_{c1}$	$\lambda_c, \overline{\lambda}_c$	λ_3, λ_4	λ_5, λ_6
$(24, 32)$	534.11	$0.9771 \pm i0.2126$	$0.2823 \pm i0.8483$	$0.5518 \pm i0.5434$
$(48, 64)$	534.07	$0.9771 \pm i0.2128$	$0.2822 \pm i0.8483$	$0.5514 \pm i0.5443$

Secondary Transition

(N_c, K)	$\mathcal{R}_{c2}$	$\lambda_c, \overline{\lambda}_c$	λ_3	λ_4, λ_5
$(24, 32)$	595.6	$0.654 \pm i0.756$	-0.949	$-0.477 \pm i0.813$
$(48, 64)$	594.8	$0.662 \pm i0.750$	-0.948	$-0.476 \pm i0.811$

Tertiary Transition

(N_c, K)	$\mathcal{R}_{c3}$	$\lambda_c, \overline{\lambda}_c$	λ_3	λ_4, λ_5
$(24, 32)$	626.8	$0.100 \pm i0.995$	-0.879	$0.386 \pm i0.266$
$(48, 64)$	629.4	$0.137 \pm i0.991$	-0.934	$0.386 \pm i0.296$

$\delta\mathcal{R} = 1$. Each point on the branch is validated by integration over the full period τ_w of the solution; each point on the branch is a wave of constant amplitude and is a fixed point of the map Φ_{τ_w} to an error of less than 10^{-4} in the infinity norm. A secant method to a tolerance of 10^{-2} in the parameter $\mathcal{R}$ is used to locate the bifurcation point $\mathcal{R} = \mathcal{R}_{c2}$.

Using the method described in Section IV C, the preconditioner is computed at $\mathcal{R} = 560$, with $\mathbf{u}$ taken as the initial guess for the corresponding point on the branch of rotating wave solutions. This preconditioner is used for the entire rotating wave solution branch. The time step $\delta t_P = 1 \times 10^{-3}$ is used for the computation of the preconditioner. This value is chosen to maximize efficiency, while still enabling convergence. In particular, choosing a $\delta t_P > 10^{-3}$ does not produce an effective preconditioner, while choosing it smaller does not significantly improve the effectiveness. The parameter value for the arbitrary computation time used for the computation of the rotating waves (i.e. of the flow map Φ_t) is chosen as $t = 0.1$. Changes in this value did not affect any of the results.

As an accuracy check, eigenvalues have been computed at $\mathcal{R} = 590$ using a grid size

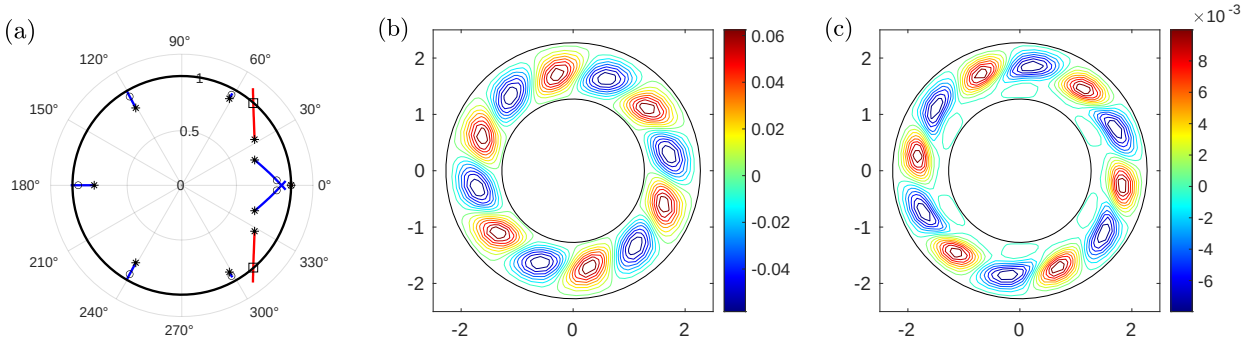

FIG. 4. Eigenvalues and critical eigenfunction along rotating wave branch. (a) The evolution of the largest magnitude eigenvalues of the linearization of the map Φ_{τ_w} along the solution branch of the rotating waves; the 10 largest eigenvalues with respect to modulus are depicted for Rayleigh number $560 \leq \mathcal{R} \leq 614$. At $\mathcal{R}_{c2} = 595.6$, the critical eigenvalues are marked with a square, while the others eigenvalues are marked with a circle; all eigenvalues are marked with a star at $\mathcal{R} = 560$. (b) The real part of V_ϕ, and (c) the imaginary part of V_ϕ, where V_ϕ is the ϕ component of the eigenfunction corresponding to the critical eigenvalues at $\mathcal{R} = \mathcal{R}_{c2}$.

reduced by a factor of two (i.e. using $N_c = 48$ and $K = 64$). The reduction in grid size results in differences of at most 0.013, or less than 2%, in both the real and imaginary parts; see Table II. Mostly, the differences are much less than this. Similarly, the critical Rayleigh number with corresponding critical eigenvalue for the finer grid is shown in Table III. The difference of critical Rayleigh number $\mathcal{R}_{c2}$ on the finer grid is 0.8, or approximately 0.13%.

C. Amplitude-modulated waves and the tertiary transition

Along the branch of rotating waves, a secondary bifurcation is detected at a critical Rayleigh number $\mathcal{R}_{c2} = 595.6$, where again a complex conjugate pair of eigenvalues of $D_{\mathbf{u}}\Phi_{\tau_w}$ crosses the $|z| = 1$ curve in the complex plane, while for $\mathcal{R}_{c1} < \mathcal{R} < \mathcal{R}_{c2}$, all eigenvalues have modulus 1 or less [45]; see Figure 4. The bifurcation of the map Φ_{τ_w} at $\mathcal{R} = \mathcal{R}_{c2}$ is supercritical and of type Neimark-Sacker. In this case, the bifurcating solution lies on a 2-torus in the corresponding continuous-time phase space. In terms of the physical quantities, because the eigenfunction corresponding to the critical eigenvalue, shown in Figure 4, resembles a wave with the same azimuthal wave number as the rotating wave undergoing the bifurcation, we expect that the bifurcating solution is an amplitude-

modulated wave (also referred to as amplitude vacillating wave). We confirm this using simulations of the initial value problem. These solutions resemble a rotating wave with wave number six (see Figure 3) whose amplitude oscillates periodically in time, except that there is a slight tilting of the vortices when the amplitude is at its lowest. See Supplemental Material [46] for an animation of the stream function deviation $\phi^{(1)}$ corresponding to the amplitude-modulated rotating wave solution at $\mathcal{R} = 620$. Generally, the solutions are quasi-periodic. That is, although the solution at the end of a period of the amplitude oscillations is a rotated version of the solution at the beginning of the period, it never quite returns to its starting point, regardless of the number of periods of amplitude oscillation. This occurs because, generally, the ratio of the frequency of amplitude oscillations to the frequency of the oscillations due to the rotating wave, is irrational. However, this ratio is expected to vary smoothly with the parameters [6], and therefore, at isolated points along the solution branch, in particular when the ratio of frequencies is rational, the solution is periodic. In this case, there are an infinite number of periodic solutions; phase shifts of the periodic solution at any point in time correspond to other periodic solutions. This property of the solutions is not a generic property of general dynamics on 2-tori, but is a consequence of the rotational symmetry [6, 43].

We continue the amplitude-modulated waves in $\mathcal{R} > \mathcal{R}_{c2}$ by solving (28) using Newton iteration with natural continuation, i.e. with $\mathcal{R}$ fixed at each point along the solution branch [47]. Initial guesses of the first two points on the solution branch are found from time-integration of a random initial guesses at $\mathcal{R} = 620$ and 620.25. As in the case for the rotating waves, for this value of the parameter, time-integration leads to sufficient decay of transients because the solution is stable. Initial guesses for all other points along the curve are found by following a secant to the solution branch which is computed from the previous two points along the branch. Relative to the rotating wave case, smaller increments of $\delta\mathcal{R} = 1/4$ in the parameter along the solution branch are required to obtain adequate initial guesses for the Newton iteration to converge. In addition, it is necessary to recompute preconditioning matrices every several steps along the solution branch. Also, a reduced time-step of $\delta t_P = 5\times10^{-4}$ is required to produce an effective preconditioner. These factors, along with the requirement that the integration time be the period τ of the amplitude oscillations, lead to a significantly more intensive computational task, relative to the computation of the rotating waves. For this reason, we choose a time-step for the time-stepper to be $\delta t =$

2×10^{-4}. Tests show that this increase in the time-step introduced errors in the eigenvalues of less than 0.1%.

Each point on the branch of amplitude-modulated wave solutions is a fixed point of the map $\gamma^{-1}\Phi_\tau$ to an error of less than 10^{-4} in the infinity norm. We validate points on the branch as an amplitude-modulated wave by using them as initial data for the time-stepper, integrated over a period τ, and confirming that the amplitude of the observed rotating wave undergoes a single period of oscillation; see Figure 5(a). At each point on the branch, a maximum and minimum of the wave amplitude of the stream function deviation are found from the results of this time-stepper integration. These are plotted in the bifurcation diagram of Figure 2. It can be seen that the range of the wave amplitude grows quickly as $\mathcal{R}$ is increased from $\mathcal{R}_{c2} = 595.6$, then as the minimum amplitude approaches zero, begins to grow more slowly. Figure 5 shows the variation of the amplitude (spatial maximum of the absolute value of the stream function deviation $\phi^{(1)}$) as a function of time over a single period of the amplitude oscillation, as well as the period of the amplitude oscillations as $\mathcal{R}$ is varied. The phase speed w (not shown) decreases monotonically from 5.05 at $\mathcal{R} = 600$ to 4.72 at $\mathcal{R} = 635$, where, initially, the slope is relatively flat but becomes steeper as $\mathcal{R}$ is increased. For values of the parameter close to the bifurcation ($\mathcal{R}_{c2} = 595.6 < \mathcal{R} < 600$), errors are introduced to the calculation of the phase speed and period of amplitude oscillation due to the small variation of amplitude over the period of oscillation coupled with the spatial and temporal discretization. As such, we do not plot these values in Figure 5(b).

The stability of the amplitude-modulated waves is found from the spectrum of $\gamma^{-1}D_{\mathbf{u}}\Phi_\tau$, where τ is the period of the amplitude oscillations and γ is the rotation operator through angle $\theta = w\tau$ (see Section IV D). The 12 eigenvalues with largest magnitude are computed at each point along the branch; their dependence on $\mathcal{R}$ is plotted in Figure 6. Application of the secant method finds a tertiary transition at $\mathcal{R}_{c3} = 626.8$; see Figure 2. There is also a short interval of instability along the branch of amplitude-modulated waves that occurs at $\mathcal{R} = 608$. Time-stepping simulations taken in the small region of instability produce solutions that are indistinguishable from those taken in neighbouring stable regions. This suggests that a supercritical bifurcation occurs and the bifurcating solution does not grow significantly before again coalescing with the branch of amplitude-modulated waves. Variation in a second parameter would be necessary to investigate this further; we leave this for future study.

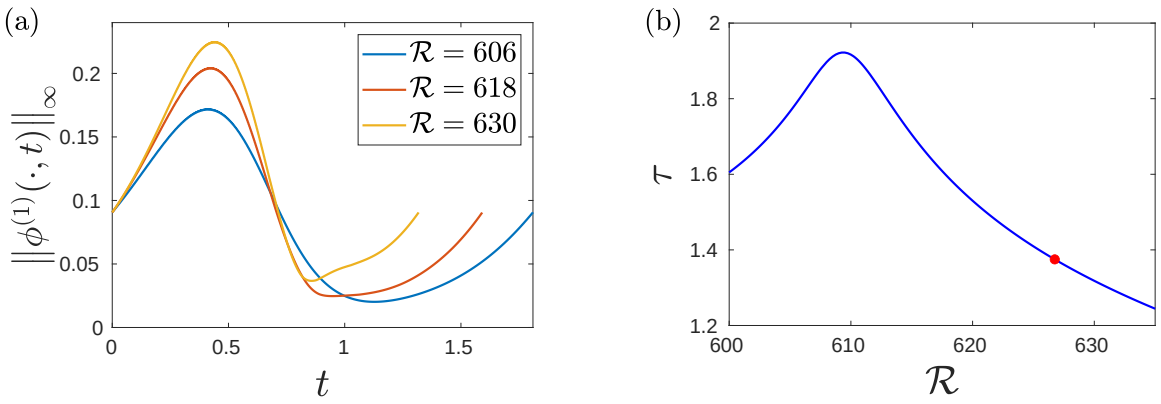

FIG. 5. Amplitude-modulated rotating wave. (a) $\left\|\phi^{(1)}(\cdot,t)\right\|_\infty$, the infinity norm of the stream function deviation at a particular time (spatial maximum of $|\phi^{(1)}|$), i.e. the wave amplitude, as a function of time t over one period of the amplitude oscillations; results for three different values of the Rayleigh number $\mathcal{R}$ are plotted. (b) The period τ of the amplitude oscillations as a function of $\mathcal{R}$; the dot indicates the period at $\mathcal{R} = \mathcal{R}_{c3} = 626.8$.

In order to verify the computations, the eigenvalues have been computed for $\mathcal{R} = 629$ on a grid with $Nc = 48$ and $K = 64$; see Table II. The largest discrepancy between the computations on the two grids is 0.027, or approximately 7%. This, however, is in the real part of the eigenvalue with sixth largest magnitude; all others are similar to less than approximately 4%. The critical Rayleigh number $\mathcal{R}_{c3}$ has also been computed on the finer grid; see Table III. The computations for $\mathcal{R}_{c3}$ on the different grids show a difference of 2.6, or approximately 0.4%.

The linear stability analysis reveals that a Neimark-Sacker bifurcation of the map $\gamma^{-1}\Phi_\tau$ occurs as a complex conjugate pair of eigenvalues crosses the $|z| = 1$ curve in the complex plane, while all other eigenvalues have magnitude less than or equal to 1 [48]. For a Neimark-Sacker bifurcation, to first order, the bifurcating solution is the stationary solution of the map plus a perturbation that is a linear combination of the real and imaginary parts of the critical eigenfunction. Generically, the specific linear combination will be different on each iteration of the map, and will depend on the critical eigenvalue and parameter. The corresponding solution for the continuous time case must coincide with this solution after each interval of the period τ, specifically, in a frame of reference following the flow (i.e. rotating at the phase speed ω). Here, the critical eigenfunction, associated with the critical eigenvalue $\lambda_1 = 0.100 + i0.995$, looks like a wave with wave number 5, but with two pairs of cells

elongated relative to the other cells; see Figure 6. The cells that are not elongated appear to have the same size as those with azimuthal wave number 6, while the elongated cells are approximately twice as large. Thus, it resembles a wave with wave number 6, multiplicatively coupled to one with wave number 1. The imaginary part of the eigenfunction resembles the real part, but rotated by an angle of approximately $\pi/2$. As such, linear combinations of the real and imaginary parts of the eigenfunction (and therefore, the perturbation from the amplitude-modulated wave associated with the bifurcating solution), will resemble a wave of azimuthal wave number 6, whose amplitude varies with the azimuthal variable.

Because the nodal lines of the real and imaginary parts of the eigenfunctions coincide, the azimuthal phase of this wave is the same for all possible linear combinations. This implies that after each iteration of the map $\gamma^{-1}\Phi_\tau$, the perturbation has the same phase as the amplitude-modulated wave, i.e., it is phase-locked with the amplitude-modulated wave, or, possibly has some integer multiple of the phase speed. If the perturbation is phase-locked, the form of the perturbation ensures that, at any given time, it will constructively interfere with the amplitude-modulated wave on one side of the annulus and destructive on the other side. Generically, the amplitude of the perturbation varies at a distinct frequency, and thus, the bifurcating solution corresponds to a 3-frequency flow that breaks the discrete rotational symmetry.

Although linear analysis can determine the parameter value at which a bifurcation occurs, and, to first order, the form of the bifurcating solutions, it cannot determine the stability of the bifurcating solutions, or the regions in parameter space in which they exist (i.e. whether the bifurcation is super-critical or sub-critical). In fact, the solution may be dynamically, or structurally, unstable. A weakly nonlinear analysis could provide further information. However, it is not guaranteed to provide results that extend sufficiently far from the bifurcation point, and such an analysis is a very large computational task. Therefore, we leave this for possible future study, and, consequently, the branch of solutions emanating from the tertiary bifurcation is not plotted in the bifurcation diagram of Figure 2. Here, we confirm our predictions with a comparison with simulations of the initial value problem (i.e. time-stepping). In particular, simulations at values of the Rayleigh number slightly larger than the critical value $\mathcal{R}_{c3}$, reveal a flow consistent with the occurrence of a supercritical Neimark-Sacker bifurcation, i.e. we observe a stable bifurcating solution of the form predicted from the linear stability computations discussed above. See Supplemental Material [49] for an animation of

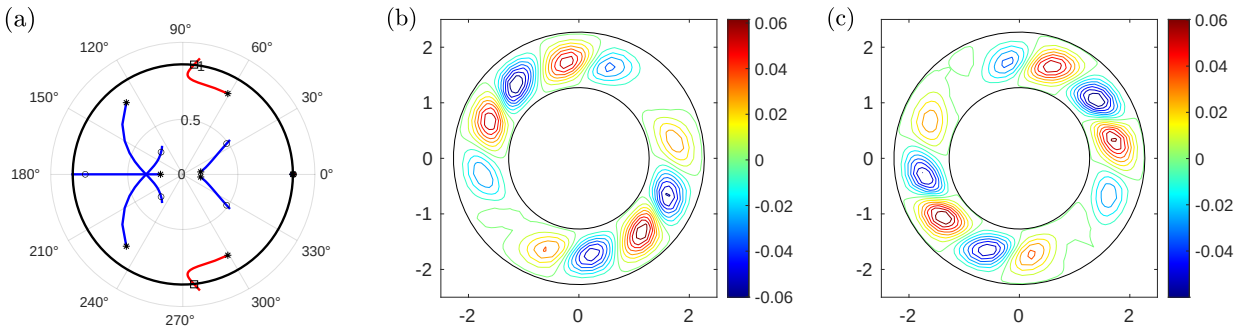

FIG. 6. Eigenvalues and critical eigenfunction along branch of amplitude-modulated waves. (a) The evolution of the largest magnitude eigenvalues of $\gamma^{-1}D_{\mathbf{u}}\Phi_\tau$ along the solution branch of the amplitude-modulated rotating waves; the 9 largest eigenvalues with respect to modulus are depicted for Rayleigh number $611 \leq \mathcal{R} \leq 631$. At $\mathcal{R}_{c3} = 626.8$, the critical eigenvalues are marked with a square, while the others eigenvalues are marked with a circle; all eigenvalues are marked with a star at $\mathcal{R} = 611$. (b) The real part of V_ϕ, and (c) the imaginary part of V_ϕ, where V_ϕ is the ϕ component of the eigenfunction corresponding to the critical eigenvalues at $\mathcal{R} = \mathcal{R}_{c3}$.

the stream function deviation $\phi^{(1)}$ corresponding to the solution at $\mathcal{R} = 629$.

It is interesting to note that this tertiary transition may lie close to a strong 1:4 resonant bifurcation, i.e. it may be possible to vary a second parameter in such a way that the critical eigenvalue (which for the current choice of parameters is $\lambda_1 = 0.100 + i0.995$) becomes purely imaginary. Near such a bifurcation, frequencies may synchronize resulting in a period-4 flow. Furthermore, there is a rich variety of other behaviour that may be seen near such a bifurcation, including period-4 cycles and heteroclinic connections [43]. We leave the localization of the bifurcation and analysis of the resonance to future study.

The three-frequency flow is observed in simulations throughout the interval $628 < \mathcal{R} < 632$; we expect that these solutions persist down to $\mathcal{R}_{c3}$, but, as previously mentioned, we do not perform a weakly nonlinear analysis to prove this. Near $\mathcal{R} = 632$, the simulations produce a flow that resembles an amplitude-modulated rotating wave with an amplitude that oscillates twice before returning to its initial amplitude; see Figure 7 and Supplemental Material [50] for an animation of the stream function deviation $\phi^{(1)}$ corresponding to this solution at $\mathcal{R} = 632$. This pattern is repeated throughout the duration of the simulation (i.e. over 40 cycles). We will refer to this flow as a period-two amplitude-modulated wave. The initial conditions for the simulations are taken to be the end point of the simulation at

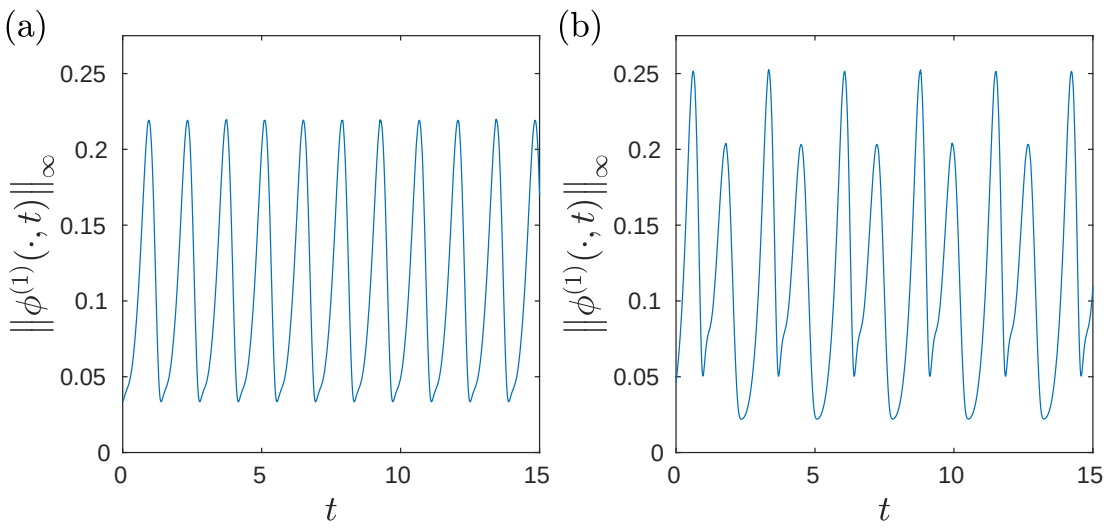

FIG. 7. $\left\|\phi^{(1)}(\cdot,t)\right\|_\infty$, the infinity norm of the stream function deviation (spatial maximum of $|\phi^{(1)}|$), i.e. the wave amplitude, as a function of time t (a) stable amplitude-modulated rotating wave at $\mathcal{R} = 626$ (before transition at $\mathcal{R}_{c3}$); (b) period-2 amplitude-modulated rotating wave at $\mathcal{R} = 631.7$. See Supplemental Material [46] and [50] for respective animations of the stream function deviation $\phi^{(1)}$.

the previously computed Rayleigh number, and we visualize solutions only for $t > 100$ to ensure that transients have been dampened.

If this period-2 flow is an amplitude-modulated wave resulting from a period doubling bifurcation, then the system (28), involving the map Φ_τ, can be used to compute them directly. We show that this is the case, starting at a Rayleigh number of $\mathcal{R} = 632$, following the same procedure as discussed at the beginning of this section. In this case, it is necessary to use smaller increments $\delta\mathcal{R} = 1/10$ of the parameter along the solution curve to obtain adequate initial guesses for the Newton iteration to converge. In addition, it is necessary to recompute preconditioning matrices every second step along the solution branch.

It is found that this period-2 flow results from a period-doubling bifurcation of the original amplitude-modulated rotating wave at $\mathcal{R} = 630.6$, i.e. at the bifurcation, there is a single $\lambda = -1$ eigenvalue. The corresponding eigenfunction is real and resembles a wave with azimuthal wave number six. The bifurcating flow is unstable at transition, as the flow originates from one that is already unstable. However, at $\mathcal{R} = 631.4$, it becomes stable for a small interval of $\mathcal{R}$. Namely, the bifurcating flow again becomes unstable at $\mathcal{R} = 632.0$.

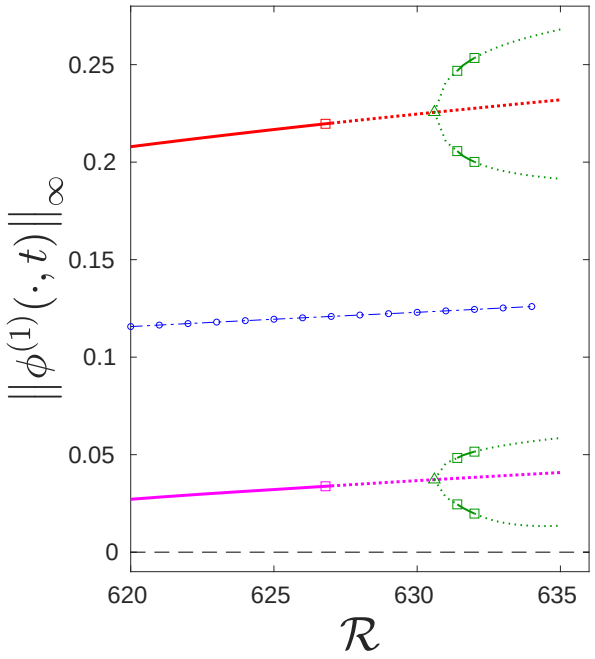

FIG. 8. The bifurcation diagram (enlargement of region around the bifurcation at $\mathcal{R}_{c3} = 626.8$). Solutions are represented in terms of $\left\|\phi^{(1)}(\cdot,t)\right\|_\infty$, the infinity norm of the stream function deviation at a particular time (spatial maximum of $|\phi^{(1)}|$), i.e. the wave amplitude. For the period-2 amplitude-modulated rotating waves, the higher and lower maximum, as well as the higher and lower minimum amplitude of the solution over a period of the amplitude oscillations are plotted in green (lightest). The triangle represents the period-doubling bifurcation at $\mathcal{R} = 630.6$, and the squares at $\mathcal{R} = 631.4$ and $\mathcal{R} = 632.0$ delineate the region of stability of the period-2 flow. Values for other parameters are listed in Table I.

The period-2 amplitude-modulated waves are represented in the bifurcation diagram in Figure 2, while Figure 8 shows the relevant region of Figure 2 blown-up to highlight these new solutions.

At the $\mathcal{R} = 632.0$ transition, the critical eigenvalues of the map $\gamma^{-1}\Phi_\tau$ are a complex conjugate pair (in particular $\lambda_c = -0.2527 \pm 0.9675i$), suggesting that the bifurcating solution will again be a three-frequency flow. Simulations of the initial value problem suggest that this is the case. In particular, for $\mathcal{R} > 632$, an apparent three-frequency flow is observed, which resembles the period-2 flow, but with lower frequency oscillations in the peak amplitude (see Figure 9); this is consistent with a supercritical Neimark-Sacker bifurcation of the period-2 flow at $\mathcal{R} = 632$. See also Supplemental Material [51] for an animation of the

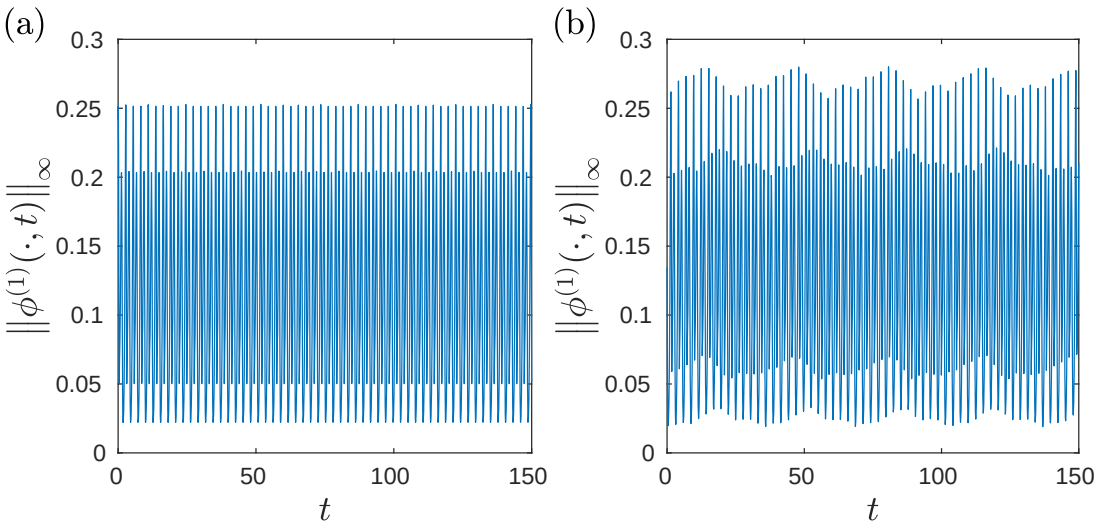

FIG. 9. $\left\|\phi^{(1)}(\cdot,t)\right\|_\infty$, the infinity norm of the stream function deviation (spatial maximum of $|\phi^{(1)}|$), i.e. the wave amplitude, as a function of time t. (a) period-2 amplitude-modulated rotating wave at Rayleigh number $\mathcal{R} = 631.7$, as in Figure 7b; (b) modulated amplitude vacillating flow at Rayleigh number $\mathcal{R} = 633$. See Supplemental Material [50] and [51] for respective animations of the stream function deviation $\phi^{(1)}$.

stream function deviation $\phi^{(1)}$ of the solution at $\mathcal{R} = 637$. This type of flow has been called modulated amplitude vacillation and has been observed in both experiment and simulation of the differentially heated rotating fluid annulus; see, e.g., [52–55].

In [55] numerical simulations of the differentially heated rotating annulus reveal a period-doubling bifurcation sequence similar to that observed in the logistic map. Our results may provide some insight into the origin of this behaviour, which warrants further investigation.

VI. CONCLUSION

In this study, we use numerical bifurcation techniques to study the flow transitions that occur in a mathematical model of sheared annular electroconvection as the electric Rayleigh number $\mathcal{R}$ is increased. A pseudo-spectral time-stepping code, that models the motion of the thin film, is used to approximate a flow map $\Phi_t(\mathbf{u})$ that gives the solution of the model equations at time t for initial conditions $\mathbf{u}$. The axisymmetric flow, rotating waves, and amplitude-modulated waves observed in the physical system, which, in the model equations,

correspond to steady solutions, limit cycles and invariant 2-tori, respectively, are computed as fixed points of this flow map. The approach exploits the fact that the rotating waves are relative equilibria, which enables the extension of such methods to the continuation of the amplitude-modulated rotating waves.

The Newton-Krylov numerical continuation and linear stability analysis that are implemented require only knowledge of the map $\Phi_t(\mathbf{u})$, and does not require access to a linearized code. That is, we consider $\Phi_t(\mathbf{u})$ as a black box, and all computations of the solutions and eigenvalues are accomplished solely by evaluations of Φ_t. This distinguishes this study from [27], the previous study that uses a similar approach to perform numerical continuation of amplitude-modulated rotating waves. This aspect may enable a more straightforward implementation on other problems.

Unlike in previous applications of similar methods [20, 27], we do not obtain reasonable convergence of the GMRES iterations, during the solution of the linear systems for the Newton iterations, without the use of a preconditioner. This may be due to the nonlocal nature of the coupling of the charge density through the 3D electric potential. Our preconditioner is naively computed as a direct approximation of the matrix involved in the linear equations, but is used for all Newton iterations across a range of parameter values. Although this preconditioner is very effective across a range of parameters, its computation may be a major contribution to the overall time of computation. However, its computation is trivially parallelizable, and therefore this issue may be easily mitigated.

The numerical methods locate a sequence of three flow transitions as the Rayleigh number $\mathcal{R}$ is increased. The primary transition, which is a transition from axisymmetric to rotating wave flow, is shown to occur at the critical Rayleigh number, $\mathcal{R}_{c1} = 534.1$, with a critical azimuthal wave number, $m_c = 6$, for the parameters in Table I. These results are in agreement with those obtained experimentally [11, 12], analytically [10, 32], and using direct numerical simulation [14, 15, 17]. The secondary transition to the amplitude-modulated waves is identified at $\mathcal{R}_{c_2} = 595.6$, which also compares quantitatively to previous studies that have used direct numerical simulation [14, 17]. The tertiary transition occurs at $\mathcal{R}_{c_3} = 626.8$, as the amplitude-modulated waves lose stability to a three-frequency flow. Also, along the solution branch of the amplitude-modulated waves, we find a period-doubling bifurcation at $\mathcal{R}_{c_4} = 630.6$, which gives rise to an amplitude-modulated wave whose period of amplitude oscillation is twice that of the original solutions. These period-2 solutions transition

to a three-frequency flow previously referred to as modulated amplitude vacillation, which resembles amplitude-modulated waves but for which the amplitude oscillations are modulated [52]. The tertiary transition has not previously been identified, and the period-2 amplitude-modulated waves and modulated amplitude vacillating flows have not previously been reported. Furthermore, the analysis reveals that the primary, secondary and tertiary transitions all occur via supercritical Neimark-Sacker bifurcations, while the period-2 bifurcation, that results in the period-2 amplitude-modulated waves, is also supercritical. The form of the bifurcating flows can be explained in terms of the critical eigenfunctions.

We have confirmed all results by both qualitative and quantitative comparison to computations with a numerical grid size reduced by a factor of two.

The flows observed near the tertiary transition greatly resemble flows of interest that have been observed in various differentially heated rotating systems. In particular, we observe flows that resemble the modulated amplitude vacillation seen in [52–55], and those that result from the sequence of bifurcations observed in [55]. This presents an opportunity to study such flows, and the progression to more complex flows in general, in a two-dimensional system.

We have shown the feasibility and validity of the application of numerical bifurcation techniques to sheared annular electroconvection. This motivates the application of the method to other geophysical fluid systems, and motivates further bifurcation analysis of the electroconvection system itself, including the exploration of the effects of other nondimensional parameters (e.g. the Reynolds number Re, the aspect ration α, and the Prandtl number $\mathcal{P}$), and the study of other interesting flows that have previously been observed. Of particular interest are rotating waves consisting of isolated (localized) or elongated vortices [14, 17], because their origin and nature are not understood.

ACKNOWLEDGMENTS

M.P. thanks Peichun Tsai for sharing her code to be developed and extended. M.P. thanks Genevieve Bourgeois for her summer Master's project testing the code's convergence and performance in various regimes. G.M.L. would like to acknowledge support from the Natural Sciences and Engineering Research Council of Canada (NSERC), [funding reference number 006257]. The authors would like to thank the reviewers for their thorough and

insightful comments.

The code used for the computation of the results presented in this paper is available upon request from the corresponding author.

---

[1] R. Hide and P. Mason, Sloping convection in a rotating fluid, Adv. Geophys. **24**, 47 (1975).

[2] P. Hignett, A. A. White, R. D. Carter, W. D. N. Jackson, and R. M. Small, A comparison of laboratory measurements and numerical simulations of baroclinic wave flows in a rotating cylindrical annulus, Quart. J. Roy. Meteorolog. Soc. **111**, 131 (1985).

[3] P. Read, Transition to geostrophic turbulence in the laboratory, and as a paradigm in atmospheres and oceans, Surv. Geophys. **22**, 265 (2001).

[4] G. M. Lewis and W. Nagata, Double hopf bifurcations in the differentially heated rotating annulus, SIAM Journal on Applied Mathematics **63**, 1029 (2003).

[5] G. M. Lewis, Mixed-mode solutions in an air-filled differentially heated rotating annulus, Physica D **239**, 1843 (2010).

[6] D. Rand, Dynamics and symmetric. predictions for modulated waves in rotating systems, Archive for Rational Mechanics and Analysis **79**, 1 (1982).

[7] D. Fultz, Developments in controlled experiments on larger scale geophysical problems (Elsevier, 1961) pp. 1–103.

[8] A. Alonso, M. Net, and E. Knobloch, On the transition to columnar convection, Physics of Fluids **7**, 935 (1995), https://doi.org/10.1063/1.868569.

[9] A. Alonso, M. Net, I. Mercader, and E. Knobloch, Onset of convection in a rotating annulus with radial gravity and heating, Fluid Dynamics Research **24**, 133 (1999).

[10] Z. A. Daya, V. B. Deyirmenjian, and S. W. Morris, Electrically driven convection in a thin annular film undergoing circular Couette flow, Physics of Fluids **11**, 3613 (1999).

[11] Z. A. Daya, V. B. Deyirmenjian, and S. W. Morris, Bifurcations in annular electroconvection with an imposed shear, Physical Review E **64**, 036212 (2001).

[12] Z. A. Daya, V. B. Deyirmenjian, S. W. Morris, and J. R. De Bruyn, Annular electroconvection with shear, Physical Review Letters **80**, 964 (1998).

[13] V. B. Deyirmenjian, Z. A. Daya, and S. W. Morris, Codimension-two points in annular electroconvection as a function of aspect ratio, Physical Review E **72**, 036211 (2005).

[14] P. Tsai, Z. A. Daya, V. B. Deyirmenjian, and S. W. Morris, Direct numerical simulation of supercritical annular electroconvection, Physical Review E **76**, 026305 (2007).

[15] P. Tsai, S. W. Morris, and Z. A. Daya, Localized states in sheared electroconvection, EPL (Europhysics Letters) **84**, 14003 (2008).

[16] P. Tsai, Z. A. Daya, and S. W. Morris, Aspect-ratio dependence of charge transport in turbulent electroconvection, Physical Review Letters **92**, 084503 (2004).

[17] P.-C. Tsai, *The Route to Chaos and Turbulence in Annular Electroconvection*, Ph.D. thesis, University of Toronto (2007).

[18] M. Cross and H. Greenside, *Pattern Formation and Dynamics in Nonequilibrium Systems* (Cambridge University Press, 2009).

[19] H. Dijkstra, F. Wubs, A. Cliffe, E. Doedel, I. Dragomirescu, B. Eckhardt, A. Gelfgat, A. Hazel, V. Lucarini, A. Salinger, E. Phipps, J. Sanchez, H. Schuttelaars, L. Tuckerman, and U. Thiele, Numerical bifurcation methods and their application to fluid dynamics: Analysis beyond simulation, Communications in Computational Physics **15**, 1 (2014).

[20] J. Sánchez, M. Net, B. Garcıa-Archilla, and C. Simó, Newton–Krylov continuation of periodic orbits for Navier–Stokes flows, Journal of Computational Physics **201**, 13 (2004).

[21] J. Sánchez, M. Net, and C. Simó, Continuation of invariant tori by Newton-Krylov methods in large-scale dissipative systems, Physica D **239**, 123 (2010).

[22] L. S. Tuckerman and D. Barkley, Bifurcation analysis for timesteppers, in *Numerical Methods for Bifurcation Problems and Large-Scale Dynamical Systems*, IMA Volumes in Mathematics and its Applications, Vol. 119, edited by E. Doedel and L. Tuckerman (Springer–Verlag, 2000) Chap. 8, p. 453–466.

[23] I. Mercader, O. Batiste, and A. Alonso, Continuation of travelling-wave solutions of the Navier-Stokes equations, International Journal for Numerical Methods in Fluids **52**, 707 (2006).

[24] D. Viswanath, Recurrent motions within plane Couette turbulence, Journal of Fluid Mechanics **580**, 339 (2007).

[25] J. Sánchez, F. Garcia, and M. Net, Computation of azimuthal waves and their stability in thermal convection in rotating spherical shells with application to the study of double-Hopf bifurcation, Physical Review E **87**, 1 (2013).

[26] G. Kawahara, M. Uhlmann, and L. van Veen, The significance of simple invariant solutions in turbulent flows, Annual Review of Fluid Mechanics **44**, 203 (2012).

[27] F. Garcia, M. Net, and J. Sánchez, Continuation and stability of convective modulated rotating waves in spherical shells, Physical Review E **93**, 1 (2016).

[28] Y. Saad, *Iterative Methods for Sparse Linear Systems*, 2nd ed. (SIAM, Philadelphia, 2003).

[29] D. A. Saville, Electrodynamics: The Taylor-Melcher leaky dielectric model, Annual Review of Fluid Mechanics **29**, 27 (1997), https://doi.org/10.1146/annurev.fluid.29.1.27.

[30] S. W. Morris, J. R. de Bruyn, and A. D. May, Patterns at the onset of electroconvection in freely suspended smectic films, Journal of Statistical Physics **64**, 1025 (1991).

[31] S. S. Mao, J. R. de Bruyn, and S. W. Morris, Boundary-induced wavelength selection in a one-dimensional pattern-forming system, arXiv preprint patt-sol/9503002 (1995).

[32] Z. A. Daya, S. W. Morris, and J. R. de Bruyn, Electroconvection in a suspended fluid film: a linear stability analysis, Physical Review E **55**, 2682 (1997).

[33] V. B. Deyirmenjian, Z. A. Daya, and S. W. Morris, Weakly nonlinear analysis of electroconvection in a suspended fluid film, Physical Review E **56**, 1706 (1997).

[34] Z. A. Daya, V. B. Deyirmenjian, and S. W. Morris, Sequential bifurcations in sheared annular electroconvection, Physical Review E **66**, 015201 (2002).

[35] M. S. Feiz, R. M. Namin, and A. Amjadi, Theory of the liquid film motor, Phys. Rev. E **92**, 033002 (2015).

[36] R. Peyret, *Spectral Methods for Incompressible Viscous Flows*, Vol. 148 (Springer, New York, 2002).

[37] J. Varah, Stability restrictions on second order, three level finite difference schemes for parabolic equations, SIAM Journal on Numerical Analysis **17**, 300 (1980).

[38] U. Ascher, S. Ruuth, and B. Wetton, Implicit-explicit methods for time-dependent partial differential equations, SIAM Journal on Numerical Analysis **32**, 797 (1995).

[39] In [17], the stream function was split into base state and deviation parts, $\phi = \phi^{(0)} + \phi^{(1)}$. Then $\phi^{(0)}$ was treated exactly, while the boundary conditions on the deviation part were assumed to be $\phi^{(1)}(r_i, \theta) = \phi^{(1)}(r_o, \theta) = 0$. The ODE (10) was neither derived nor time-stepped. This is equivalent to setting $g^{(1)}(t) = 0$. We can quantify the accuracy of this approximation by using our results from section V to numerically calculate the fraction $f = \max(g^{(1)}(t))/\max(g(t))$ for the various states observed. Referring to figure 2, we find that at $\mathcal{R} = 600$, in the rotating wave regime, $f \approx 3 \times 10^{-5}$, while at $\mathcal{R} = 660$, in the amplitude modulated regime, $f \approx 10^{-4}$. Thus, the simplifying approximation used in [17] is reasonably good, so that no qualitative differences

are to be expected between our calculations and theirs. This approximation amounts to adding an additional physical constraint that the part of the total azimuthal flux not imposed by the rotation of the inner electrode must be zero. As the electrical forces are mainly radial, they evidently do not produce much additional azimuthal flux.

[40] Y. Saad and M. H. Schultz, GMRES: A generalized minimal residual algorithm for solving nonsymmetric linear systems, SIAM Journal on Scientific and Statistical Computing **7**, 856 (1986).

[41] L. N. Trefethen and D. Bau III, *Numerical Linear Algebra*, Vol. 50 (SIAM, Philadelphia, 1997).

[42] R. B. Lehoucq, D. C. Sorensen, and C. Yang, *ARPACK Users' Guide: Solution of Large-Scale Eigenvalue Problems with Implicitly Restarted Arnoldi Methods* (SIAM, Philadelphia, 1998).

[43] Y. A. Kuznetsov, *Elements of Applied Bifurcation Theory*, 2nd ed., Vol. 112 (Springer Science & Business Media, 1998).

[44] (), See Supplemental Material at [URL for Movie1_Ra560_RotatingWave.mp4 will be inserted by publisher] for an animation of the stream function deviation $\phi^{(1)}$ corresponding to the rotating wave solution at $\mathcal{R} = 560$.

[45] Because $\gamma\mathbf{u}$ is a nontrivial fixed point of the map Φ_{τ_w}, the spectrum of $D_{\mathbf{u}}\Phi_{\tau_w}$ always contains at least one (real) eigenvalue equal to 1.

[46] (), See Supplemental Material at [URL for Movie2_Ra620_AmplitudeModulated.mp4 will be inserted by publisher] for an animation of the stream function deviation $\phi^{(1)}$ corresponding to the amplitude modulated wave solution at $\mathcal{R} = 620$.

[47] The code used for the computation of the results presented in this section is available upon request from the corresponding author.

[48] Because $\mathbf{u}$ is a fixed point of the map $\gamma^{-1}\Phi_{\tau_w}$, the spectrum of $D_{\mathbf{u}}\Phi_{\tau}$ always contains at least two eigenvalues equal 1, one associated with the phase of the wave and one with the phase of the amplitude oscillation.

[49] (), See Supplemental Material at [URL for Movie3_Ra629_3F.mp4 will be inserted by publisher] for an animation of the stream function deviation $\phi^{(1)}$ corresponding to the solution at $\mathcal{R} = 629$.

[50] (), See Supplemental Material at [URL for Movie4_Ra632_AmplitudeModulated_PD.mp4 will be inserted by publisher] for an animation of the stream function deviation $\phi^{(1)}$ corresponding to the (period-doubled) amplitude modulated solution at $\mathcal{R} = 632$.

[51] (), See Supplemental Material at [URL for Movie5_Ra637_ModulatedAmpVac.mp4 will be inserted by publisher] for an animation of the stream function deviation $\phi^{(1)}$ corresponding to the modulated amplitude vacillating solution at $\mathcal{R} = 637$.

[52] W.-G. Früh and P. Read, Wave interactions and the transition to chaos of baroclinic waves in a thermally driven rotating annulus, Philosophical Transactions of the Royal Society of London, A **355**, 101 (1997).

[53] A. Randriamampianina, W.-G. Früh, P. Read, and P. Maubert, Direct numerical simulations of bifurcations in an air-filled rotating baroclinic annulus, J. Fluid Mech. **561**, 359 (2006).

[54] A. Castrejon-Pita and P. Read, Baroclinic waves in an air-filled thermally driven rotating annulus, Physical Review E **75**, pp. 10 (2007).

[55] R. Young and P. Read, Flow transitions resembling bifurcations of the logistic map in simulations of the baroclinic rotating annulus, Physica D **237**, 2251 (2008).